AD-777 385

COMPRESSIBLE TURBULENT SKIN FRICTION ON ROUGH AND ROUGH/WAVY WALLS IN ADIABATIC FLOW

Daniel C. Reda

Naval Ordnance Laboratory
White Oak, Maryland

12 February 1974

DISTRIBUTED BY:

NTIS

National Technical Information Service
U. S. DEPARTMENT OF COMMERCE
5285 Port Royal Road, Springfield Va. 22151

AD777385

NOLTR 74-34

NOL TECHNICAL REPORT

COMPRESSIBLE TURBULENT SKIN FRICTION ON ROUGH AND ROUGH/WAVY WALLS IN ADIABATIC FLOW

BY
Daniel C. Reda

12 FEBRUARY 1974

NAVAL ORDNANCE LABORATORY
WHITE OAK, SILVER SPRING, MD. 20910

- Approved for public release; distribution unlimited

D D C
RECEIVED
APR 19 1974
B

NAVAL ORDNANCE LABORATORY
WHITE OAK, SILVER SPRING, MARYLAND 20910

Reproduced by
NATIONAL TECHNICAL
INFORMATION SERVICE
U S Department of Commerce
Springfield VA 22151

68

UNCLASSIFIED

SECURITY CLASSIFICATION OF THIS PAGE (When Data Entered)

REPORT DOCUMENTATION PAGE		READ INSTRUCTIONS BEFORE COMPLETING FORM
1. REPORT NUMBER NOLTR 74-34	2. GOVT ACCESSION NO.	3. RECIPIENT'S CATALOG NUMBER AD 777 385
4. TITLE (and Subtitle) COMPRESSIBLE TURBULENT SKIN FRICTION ON ROUGH AND ROUGH/WAVY WALLS IN ADIABATIC FLOW		5. TYPE OF REPORT & PERIOD COVERED
		6. PERFORMING ORG. REPORT NUMBER NOLTR 74-34
7. AUTHOR(s) DANIEL C. REDA		8. CONTRACT OR GRANT NUMBER(s)
9. PERFORMING ORGANIZATION NAME AND ADDRESS NAVAL ORDNANCE LABORATORY WHITE OAK, SILVER SPRING, MARYLAND 20910		10. PROGRAM ELEMENT, PROJECT, TASK AREA & WORK UNIT NUMBERS SSPO-77402/B1509001
11. CONTROLLING OFFICE NAME AND ADDRESS STRATEGIC SYSTEMS PROJECT OFFICE DEPARTMENT OF THE NAVY WASHINGTON, D. C. 20390		12. REPORT DATE 12 February 1974
		13. NUMBER OF PAGES 66
14. MONITORING AGENCY NAME & ADDRESS (if different from Controlling Office)		15. SECURITY CLASS. (of this report) UNCLASSIFIED
		15a. DECLASSIFICATION/DOWNGRADING SCHEDULE

16. DISTRIBUTION STATEMENT (of this Report)

APPROVED FOR PUBLIC RELEASE; DISTRIBUTION UNLIMITED.

17. DISTRIBUTION STATEMENT (of the abstract entered in Block 20, if different from Report)

18. SUPPLEMENTARY NOTES

19. KEY WORDS (Continue on reverse side if necessary and identify by block number)

TURBULENT BOUNDARY LAYERS; COMPRESSIBLE; SKIN FRICTION; ROUGHNESS; WAVY WALL; VELOCITY PROFILE

20. ABSTRACT (Continue on reverse side if necessary and identify by block number)

An experimental program was conducted to investigate effects of roughness, and roughness superimposed on single and/or multiple, shallow, periodic waveforms, on turbulent boundary-layer skin friction and velocity profile, in compressible, adiabatic flow. Test conditions were $M_\infty = 2.9$ and $Re_\infty/ft = 2$ to 8×10^6. The planar models included smooth, sand-grain, machined and molded (fiber glass-wound motor case) surface finishes. Direct

DD FORM 1 JAN 73 1473 EDITION OF 1 NOV 65 IS OBSOLETE
S/N 0102-014-6601

UNCLASSIFIED

SECURITY CLASSIFICATION OF THIS PAGE (When Data Entered)

measurements of surface shear and Pitot/recovery temperature profiles were obtained. Results show that rough/multiple periodic waveform surfaces experience higher shear than either rough and/or rough/single periodic waveform surfaces. Favorable comparisons with Goddard's skin-friction correlation, the law-of-the-wall and velocity defect correlations were found.

NOLTR 74-34 12 February 1974

COMPRESSIBLE TURBULENT SKIN FRICTION ON ROUGH AND ROUGH/WAVY WALLS IN ADIABATIC FLOW

This report summarizes a detailed investigation into the effects of roughness and roughness plus waviness on turbulent boundary-layer skin friction and velocity profile in compressible, adiabatic flow.

This work was performed under sponsorship of the Navy's Special Projects Office, in support of the Trident missile program under Task No. SSPO-77402/B1509001.

The author wishes to acknowledge the skills of Mr. M. A. Brown, for model and balance design, and Messrs. F. W. Brown and F. C. Kemerer for their efficient operation of the facility and preparation of instrumentation.

ROBERT WILLIAMSON II
Captain, USN
Commander

Leon H Schindel

LEON H. SCHINDEL
By direction

CONTENTS

		Page
I	INTRODUCTION	1
II	ROUGHNESS MODELS	3
III	EXPERIMENTAL APPARATUS AND TECHNIQUES	5
IV	RESULTS AND COMPARISONS WITH EXISTING DATA	11
	A. Smooth Wall Boundary-Layer Characteristics	11
	B. Surface Shear Stress Measurements	14
	C. Smooth and Rough Wall Temperature Profiles	19
	D. Smooth and Rough Wall Velocity Profiles	21
V	CONCLUSIONS	29
VI	REFERENCES	30

ILLUSTRATIONS

Figure	Title
1	Model Surface Schematic
2	Test Setup Schematic
3	Photograph of Floating Element, with Calibration Weight Applied, and Pitot Probe Installed
4	Photograph of Dual Pitot/Recovery Temperature Probe
5	Skin-Friction Balance Schematic
6	Smooth Wall Boundary-Layer Characteristics
7	Smooth Wall Sublayer Thicknesses from Measured Shear
8a-d	Smooth Wall Velocity Profiles
9a-c	Smooth And Rough Wall Skin-Friction Coefficients
10	Equivalent Sand-Grain Roughness Determination for Motor Case Material
11	Smooth Wall Skin-Friction Coefficients; A Comparison with Published Data
12	Smooth-to-Rough Wall Skin-Friction Coefficient Ratio vs Roughness Reynolds Number; A Comparison with Published Data
13	Smooth and Rough Wall Recovery Temperature Profiles
14a-b	Smooth and Rough Wall Temperature-Velocity Relationships
15	Effective y Origin Schematic
16	Effective y Origin Definition
17	Velocity Defect Correlation, Smooth and Rough Wall Data; A Comparison with Published Data
18a-c	Smooth and Rough Wall Velocity Profiles in Law-of-the-Wall Coordinates
19	Roughness-Induced Law-of-the-Wall Velocity Shift vs Roughness Reynolds Number; A Comparison with Published Data

TABLE

Table	Title
1	Summary of Models Tested

SYMBOLS

A,B,C,D	constants and/or coefficients in various mathematical expressions
c	speed of sound
C_f	skin-friction coefficient, $\frac{\tau_w}{\frac{1}{2}\rho_\infty u_\infty^2}$
C_{f_o}	smooth wall skin-friction coefficient
k	roughness dimension, peak-to-valley
M	Mach number
p	pressure
P_o	stagnation pressure
Re/ft.	unit Reynolds number, $\frac{\rho_\infty u_\infty}{\mu_\infty}$
Re_k	roughness Reynolds number, $\frac{k u_\tau}{\nu_w}$
Re_θ	Reynolds number based on smooth wall θ, $\frac{\rho_\infty u_\infty \theta}{\mu_\infty}$
r	recovery factor, $\left[\frac{T_{aw} - T_\infty}{T_{o_\infty} - T_\infty}\right]$
R,SW,LW	roughness, short waves, long waves
T	temperature
T_o	stagnation temperature
u	velocity
u_τ	friction velocity, $\sqrt{\frac{\tau_w}{\rho_w}}$
u^+	law-of-wall coordinate, $\left(\frac{u}{u_\tau}\right)$
$\left(\frac{\Delta u}{u_\tau}\right)$	roughness induced intercept shift in law of wall
y	vertical coordinate
y^+	law-of-wall coordinate, $\left(\frac{y u_\tau}{\nu_w}\right)$

γ	ratio of specific heats
δ	boundary-layer thickness
δ^*	boundary-layer displacement thickness
δ_s	smooth wall sublayer thickness
$\varepsilon_{SW}, \varepsilon_{LW}$	short, long waveform amplitudes
θ	boundary-layer momentum thickness
$\lambda_{SW}, \lambda_{LW}$	short, long waveform wavelength
μ	viscosity
ν	kinematic viscosity
ρ	density
τ	surface shear stress

Subscripts

aw	adiabatic wall
w	at wall, or based on wall properties
∞	local free-stream condition

I INTRODUCTION

Development of advanced, high-speed aircraft, missiles and re-entry vehicles requires specialized application of scientific knowledge from many fields. One key technical area is aero-ballistics research. The present paper deals with a specific topic in this field, namely, effects of surface roughness, and roughness plus waviness, on the surface shear stress and velocity profile of a compressible, turbulent boundary layer in adiabatic flow.

Turbulent boundary-layer flows over smooth surfaces have been studied in great detail and numerous texts and papers documenting advances in the state of the art have been written

(e.g., refs. (1) through (7)). Research on effects of roughness on turbulent boundary-layer characteristics has not received the same overall level of attention. However, a core of notable experimental results has been generated in this area and a brief review is outlined below.

The works of Nikuradse[8], for incompressible flow, and Goddard[9], for compressible flow, provided an early basis concerning effects of roughness on the skin friction and velocity profile of a fully developed turbulent boundary layer. Results substantiating and extending the findings of these classic studies have been reported by other investigators (e.g., refs. (10) to (15)). Combined interactions of surface roughness, skin friction, and heat ransfer have also been studied (e.g., refs. (16) to (22)). Based on such experimental evidence, semi-empirical prediction techniques for turbulent heat-transfer rates in the presence of surface roughness have been formulated (e.g., refs. (23) to (29)).

Along similar lines, effects of surface waviness on turbulent boundary-layer characteristics have been studied both theoretically and experimentally (e.g., refs. (30) to (35)); in all cases, however, the wavy surfaces under consideration were aerodynamically smooth, i.e., with respect to superimposed roughness.

Turbulent boundary-layer flows over surfaces which possess a roughness pattern, simultaneously superimposed on one or more periodic waveforms (i.e., rough/wavy walls), have yet to be investigated. The present paper addresses this problem for

the case of adiabatic flow. This research was motivated by an ongoing missile development program, from which both the need for such information, and its unavailability, were identified.

Current submarine-launched ballistic missiles possess motor cases made of a fiber glass-wound material. Surface ridges, or grooves, plus any surface undulations created during the fabrication process are everywhere transverse to the local flow direction. Such multistage-boost vehicles have a large percentage of their surface area covered with such waves and grooves.

During recent flight tests, range reductions were experienced which could not be accounted for by original drag calculations. It was felt that the random rough/wavy surface pattern of these motor cases was, in some manner, amplifying skin-friction drag levels beyond estimates based strictly on the smallest roughness dimension, the filament radius.

An experimental program was thereby formulated to investigate turbulent flows over such complex surface patterns.

II ROUGHNESS MODELS

Surface contour traces taken from an actual motor case section showed the existence of three dominant features, i.e., physical scales, (1) a roughness scale, (2) a short wavelength scale, and (3) a long wavelength scale. In an attempt to simulate these features, several rough/wavy patterns were created. Figure 1 schematically shows the most complex simulation fabricated for testing, wherein roughness was superimposed on

a short wavelength waveform, both of which were superimposed on a long wavelength waveform. Table 1 summarizes the roughness models tested.

As can be seen, three general categories of models were tested, sand-grain and machined roughnesses, plus an actual mold of the roughness pattern taken directly from a full-scale motor casing.

Sand-grain models were fabricated by bonding standard, uniform-grit, sandpaper sheets on to aluminum plates. Machined models were actually fabricated by impressing the desired surface patterns on aluminum plates; this technique required the machining of steel rollers with the desired patterns which, in turn, were repeatedly traversed across the softer aluminum surfaces. Roller widths were many times the roughness dimensions, and, where appropriate, were equal to several short wavelengths, or one long wavelength. Amplitude-to-wavelength ratios generated by this technique were the order of 0.010 for the short waves and 0.005 for the long waves. All dimensions shown in Table 1 were verified through optical/photographic techniques and surface contour traces (Pipe Machinery Co. contour reader, with wedge-tipped stylus 0.001 inch in thickness; system accuracy quoted at ± 0.2 mil).

Three categories of surface roughness were included in order to meet the following requirements: (1) the smooth wall model would serve as a reference case, (2) both the smooth wall and sand-grain models would serve to provide a check on present experimental apparatus/instrumentation and testing techniques through comparisons of shear and profile data with previously

published results, (3) sand-grain and molded model shear data, in combination, would serve to define equivalent sand-grain roughnesses for the motor case material, and (4) the machined roughness samples woul serve to show effects of roughness, with and without a single periodic waveform, as well as effects of simultaneously combining roughness with two periodic waveforms of differing scales.

III EXPERIMENTAL APPARATUS AND TECHNIQUES

All tests were run in the Naval Ordnance Laboratory's (NOL) Boundary Layer Channel[36], a vertical, asymmetric, variable Mach number facility, comprised of a flat nozzle wall (test surface) and a contourable nozzle wall (for variations in free-stream Mach number, pressure gradient, etc.). This facility has been used for many detailed studies of smooth wall turbulent boundary layers, e.g., references (37) to (39), and its capabilities are well documented. For this program, nominal test conditions were an edge Mach number of 2.9, nozzle stagnation pressures from 1 to 4 atm., and nozzle stagnation temperatures in the range of 582 to 592°R (see later discussion of balance temperature sensitivity), which yielded a free-stream unit Reynolds number range of 2 to 8 x 10^6/ft. For these test conditions and a constant wall temperature of 532°R, a test surface recovery factor of 0.86 was measured using a thermopile heat-transfer sensor; wall temperatures were held uniform and constant by circulating a coolant (water) through the test surface interior. All roughness tests were run under adiabatic flow conditions.

In order to adapt the present study to this facility without incorporating major modifications, the apparatus shown schematically in Figure 2 was designed. In this manner, the entire model support, balance, probe drive, etc., could be mounted to the original test surface through existing instrumentation ports. The overall height of this apparatus, above the original test surface, was the order of one boundary-layer thickness (1.0 inch), and it completely spanned the channel. The model support was located within the constant pressure region of the nozzle. A smooth, shallow five-degree ramp, followed by a five-degree expansion corner generated a new test rhombus within which the roughness samples could be mounted. The total pressure loss across the weak oblique shock wave was minimal (the order of 1/2 percent of nozzle stagnation pressure).

As noted in Figure 2, the full-span roughness samples extended over a three-foot axial length, beginning at the expansion corner. The floating element portion of each roughness sample was one foot in length, 0.5 foot in width (centered about the tunnel centerline) and its forward edge was located one foot downstream of the expansion corner. In terms of smooth wall boundary-layer thicknesses, the floating element covered an axial distance of 12.4 to 24.8 δ downstream of roughness initiation at one atm., while at four atm. the corresponding axial distances were 15.7 to 31.4 δ. Profiles were measured on centerline, at an axial station ~1.5 inches upstream of the floating element trailing edge, corresponding

to a run length over the roughness samples of 23.2 δ at one atm. (the condition at which all rough wall profiles, except one, were obtained).

Nozzle stagnation pressure and temperature, wall pressure and temperature, surface shear stress, and at least one Pitot pressure profile were measured for each roughness model (shear stress measurements were made in the absence of any probes; all profile data were obtained during separate runs). Limited recovery temperature profiles were measured to verify certain assumptions used in data reduction (see Section IV,C). All data were monitored and recorded on the existing NOL Boundary Layer Channel data system[36].

Figure 3 shows a close-up view of the smooth wall floating element section, with calibration weight applied, as installed vertically in the tunnel; the flattened tip (0.005-inch outside thickness) Pitot pressure probe can also be seen, as installed. Figure 4 shows a close-up view of the dual Pitot/recovery temperature probe used for the simultaneous measurement of these variables; the temperature probe is based on the work of Danberg[40].

Static pressure taps around the fixed periphery of the smooth wall floating element were used to check on flow uniformity. This technique is by no means conclusive; however, measured surface pressure distributions indicated essentially a zero pressure gradient flow, as desired, with spanwise Mach number uniformity within one percent of nominal and axial Mach number uniformity within two percent of nominal. Centerline edge

Mach numbers as determined from measured wall static and nozzle stagnation pressures were consistent with those values determined from measured free-stream Pitot and nozzle stagnation pressures. The degree of flow two-dimensionality achievable within this facility, for zero and nonzero pressure gradients, has been addressed in more detail previously (e.g., ref. (39)).

A detailed, cross-sectional schematic of the skin-friction balance is shown in Figure 5. Several key points concerning this instrument, and its accuracy, bear mentioning here.

The large physical size of the floating element (0.5 ft^2) was necessitated by the requirement to obtain integrated shear stress measurements over several of the longest wavelengths in question.

Each floating element sample was carefully aligned with its surroundings via the application of selected shims to the common surface between sample and balance; final alignment was verified by traversing a dial indicator/stylus across the gap between fixed and floating surfaces and by traversing a 0.005-inch feeler gage around the inside gap periphery. In addition, rough/wavy samples were fabricated and mounted such that all waveforms possessed continuity of slope at the floating element gap. Proper element alignment has been recognized as essential to the generation of accurate skin-friction data[41].

This balance was designed as a set of parallel steel planes, joined together by three pairs of steel webs; the entire structure was fabricated from a single piece of metal, i.e., the two planes and the webs were an integral unit. This design

allowed for deflections in the flow direction while maintaining the floating element everywhere parallel to the fixed baseplate (i.e., no pitching of the leading edge into and/or out of the flow was possible).

The balance was mounted to the tunnel structure at a single point, i.e., contact occurred only on the annular surface between the mounting shaft and mounting block. In addition, the facility was designed to include a plenum chamber between the test surface and the outer tunnel wall, which, during testing, is evacuated to test section pressure. These design features isolated the balance from loads which might have otherwise been transferred to it from the supporting structure.

The center pair of webs was instrumented (both surfaces) with a series of temperature-compensated strain gages; the combined output signal of these gages was used to deduce surface shear loading. A calibration (load versus millivolt output) was conducted prior to each run via the application of calibration weights (recall Fig. 3; a vertically oriented facility greatly aided in this procedure). A small hole was machined in the exact center of each floating element, in which a cylindrical pin could be mounted; known weights were then hung from this pin. Excellent linearity and repeatability were always observed during calibration (loads to ~2.5 $\#_f$, shears to ~5.0 $\#_f/ft^2$). After calibration, the pin was removed, its hole filled flush with a plaster compound, and the tunnel sealed for running.

Calibrations were always conducted with the balance and model support at room temperature; no coolant passages existed through these portions of the apparatus. Initial tests were run at a nozzle stagnation temperature which, considering the measured recovery factor of 0.86, yielded an adiabatic wall temperature of 532°R. When initial wall (i.e., test sample surface) temperature differed by more than several degrees from this preselected adiabatic wall temperature, nonnegligible heating and/or cooling of the test sample occurred prior to its reaching equilibrium (wall temperature was monitored continuously before, during, and immediately after each run; unfortunately, room temperature could not be held constant over a long time scale, i.e., from one run to the next). For such cases, unacceptable zero shifts were noted in the balance output signal (here defined as >2% of full-scale load). A test procedure was then formulated to circumvent this problem; nozzle stagnation temperature was preselected and accurately maintained (within ~2°R, via a feedback control system on the flow heater) such that adiabatic wall temperature, for each particular run, equalled the prerun wall temperature. In this manner, no appreciable thermal effects were imposed on the balance and observed zero shifts were thus held within acceptable limits (<2% of full-scale load; actually, most observations were within 1%). This, coupled with the levels of linearity and repeatability achieved during calibration, resulted in the following estimates for shear load accuracy: At the highest Re_θ levels (4 atm.), where the highest levels of shear were experienced, measurement accuracy was of the order of

three percent; at the lower Re_θ levels (1 atm.), where reduced shear levels were experienced, data accuracy was of the order of ten percent.

IV RESULTS AND COMPARISONS WITH EXISTING DATA

A. Smooth Wall Boundary-Layer Characteristics

Before presenting and discussing the bulk of the skin-friction measurements, characteristic dimensions of the reference, or smooth wall, boundary layer should be noted. Figure 6 shows momentum, mass displacement, and boundary-layer thickness as a function of free-stream unit Reynolds number. For comparison purposes, the minimum measured smooth wall momentum thickness was still nearly double the maximum roughness dimension and/or maximum wave amplitude tested.

The smooth wall boundary-layer scale of real importance for any study of roughness effects is, however, the laminar, or viscous, sublayer thickness. By combining the definition of friction velocity,

$$u_\tau = \sqrt{\frac{\tau_w}{\rho_w}} \tag{1}$$

with Newton's law of friction,

$$\tau = \mu \left(\frac{\partial u}{\partial y}\right) \tag{2}$$

or, for small y,

$$\tau_w \cong \mu_w (u/y) \tag{3}$$

the sublayer velocity distribution can be shown to be stated by

$$(u/u_\tau) = \left(\frac{y u_\tau}{\nu_w}\right) \tag{4}$$

or

$$u^+ = y^+ \tag{5}$$

Based on experimental evidence, the outer edge of the viscous sublayer occurs at a y^+ value ~11.0. Thus,

$$\delta_s = \frac{11\ \nu_w}{u_\tau} \tag{6}$$

Introducing the definitions of ν_w, u_τ, C_f, c and M into Equation (6), coupled with the assumptions of ideal gas and $p_\infty = p_w$ results in

$$\delta_s = \frac{11\ \mu_w c_w}{\gamma p_w M_\infty \sqrt{C_f/2}} \tag{7}$$

Thus, δ_s can be determined, for known P_{c_∞}, T_{o_∞} values from surface measurements of p_w, T_w and τ_w. Results so generated are shown in Figure 7.

The necessity for determining viscous sublayer thicknesses from surface measurements is best illustrated when one views an overlay of the present probe-tip dimensions on Figure 7. For an overall tip dimension of 0.005 inch, the closest point to the wall at which a velocity measurement can be claimed is 0.0025 inch, or at one-half the probe-tip height. The problem of probe tip/wall interference must then be addressed.

Figures 8a-d show present smooth wall velocity profiles in terms of (u/u_∞), (y/δ) coordinates. Both uncorrected and corrected data points are shown (probe corrections were based on earlier NOL research, e.g., Voisinet[39], and were applied to present profile data only where applicable, i.e., only for smooth wall conditions). As can be seen, these probe corrections influenced the data only in the immediate vicinity of the wall; integral parameters shown earlier in Figure 6 were computed from

the corrected velocity distributions, but any differences between those values shown in Figure 6 and values computed from the uncorrected velocity distributions were indistinguishable (third significant figure influence only).

One way to demonstrate self-consistency between present surface shear and velocity profile data is to plot sublayer velocity distributions, as determined from measured shears, on Figures 8a-d. From Equation (3),

$$\tau_w = \left[\frac{\mu_w u_\infty}{\delta}\right] \frac{(u/u_\infty)}{(y/\delta)} \tag{8}$$

or

$$(u/u_\infty) = \left[\frac{\tau_w \delta}{\mu_w u_\infty}\right](y/\delta) \tag{9}$$

On a log-log plot in these coordinates, the sublayer velocity distribution will appear as a straight line of slope equal to 45 degrees, i.e., from Equation (9),

$$\log_{10}(u/u_\infty) = \log_{10}\left[\frac{\tau_w \delta}{\mu_w u_\infty}\right] + \log_{10}(y/\delta) \tag{10}$$

or

$$u' = \text{constant} + y'$$

$$\frac{\partial u'}{\partial y'} = 1 \qquad [45° \text{ slope}]$$

and its intercept with the vertical axis used on Figures 8 will occur at

$$(u/u_\infty)_{\text{intercept}} = (0.001)\left[\frac{\tau_w \delta}{\mu_w u_\infty}\right] \tag{11}$$

Results so plotted show that, in every case, the probe-corrected velocity distribution approached the shear-determined sublayer velocity distribution in the vicinity of the wall.

Also, in every case, an extrapolation of the logarithmic region slope (profile data) to its intercept with the sublayer velocity distribution (shear data) defined a point consistent with the edge of the viscous sublayer, as determined from measured shear.

Smooth wall temperature and velocity profile data will be discussed in more detail in Sections IV, C and D, but first a presentation of all smooth and rough wall shear stress data will be made.

B. Surface Shear Stress Measurements

Figures 9a-c summarize the present skin-friction coefficient results as a function of smooth wall Re_θ. The data are subdivided into these groupings for ease in interpretation. Smooth wall coefficients are plotted on each graph for reference purposes. The smooth wall skin-friction coefficient was found to decrease with increasing Re_θ, such that $C_{f_o} \propto Re_\theta^{-0.14}$. Exponents in the range of -0.10 to -0.20 are expected for fully developed turbulent boundary layers. Repeatability of these measurements is illustrated by those two cases (smooth and molded models) wherein the models were remounted, realigned, and tested a second time.

Figure 9a shows the sand-grain results. These data are quite similar in functional dependence to the Mach 3 sand-grain results of Goddard (see Fig. 18 of ref. (9)). The 80-grit data serve especially well to illustrate the relative importance of the two dominant physical scales involved, roughness height and viscous sublayer thickness. At one atmosphere total pressure,

the viscous sublayer thickness was seven mils (Fig. 7), while roughness height was six mils, i.e., roughness peaks had not yet begun to protrude outside the sublayer. Correspondingly, no increase in skin-friction coefficient above the measured smooth wall value was observed. However, as Reynolds number was increased the viscous sublayer thinned while roughness dimension remained constant. The net result was an increase in the rough wall skin-friction coefficient above the smooth wall level. Roughness effects are thus generally subdivided into three regimes:

for $k < \delta_s$, $Re_k < 10$ or 11; aerodynamically smooth

for $\delta_s < k < 6$ or $7\ \delta_s$, $11 < Re_k < \sim 70$; transitionally rough

for $k > 6$ or $7\ \delta_s$, $Re_k > \sim 70$; fully rough

where

$$Re_k = \frac{ku_\tau}{\nu_w} = \text{roughness Reynolds number} \tag{12}$$

Figure 9b presents a subset of data which shows effects of superimposing roughness, separately, on a short, and on a long periodic waveform, as well as the effects of superimposing roughness on a surface which simultaneously possesses both a short and a long periodic waveform. For these models, k, ε_{SW}, λ_{SW}, ε_{LW} and λ_{LW} were all held constant.

Roughness as well as roughness superimposed on a short periodic waveform yielded essentially the same result. Roughness superimposed on a long periodic waveform actually showed some reduction in surface shear as compared to roughness alone. The important point, however, is that superposition of a given roughness dimension on a surface which simultaneously possessed

both short and long periodic waveforms increased surface shear above levels measured for identically rough surfaces possessing only one, or none, of these same periodic waveforms.

Figure 9c presents the final data subset, consisting of the motor case sample and three machined samples which simultaneously possessed roughness, as well as short and long wavelengths. It was hoped that these three machined samples would simulate the motor case material over different portions of its boost trajectory (by varying k, ε and λ scales versus sublayer thickness). As can be seen, the desired simulations were not achieved (models 9 and 10 should have given nearly identical results had accurate simulation been achieved). This could be due, in part, to the fact that the motor case material was of a random rough/wavy character (a fact which should be kept in mind, even though analysis of surface contour traces resulted in definition of prominent, or reoccurring, roughness and waveform dimensions, i.e., those listed in Table 1).

Increasing roughness and waveform dimensions, while maintaining nearly constant (ε/λ) ratios (~0.01 for short waves and ~0.005 for long waves) resulted in increased surface shear stresses. All three samples showed a similar functional dependence on Re_θ. On the other hand, the motor case material showed an opposite trend, with C_f decreasing slightly as Re_θ increased.

Equivalent sand-grain roughnesses for the motor case material were obtained by cross-plotting rough-to-smooth wall C_f ratios versus sand-grain height, and superimposing motor case C_f ratios on corresponding constant Reynolds number

(i.e., constant P_{O_∞}) lines. The results are shown in Figure 10. Equivalent sand-grain roughnesses for this material (5 to 10 mils) were 3.8 to 7.6 times the roughness scale attributed to it, and 1.25 to 2.5 times its ascribed short wave amplitude. As suspected, skin-friction drag calculations based solely on the smallest roughness scale were not representative of the actual situation.

This section is concluded with two comparisons between present results and previously published data. Figure 11 shows the first comparison, strictly for smooth wall data. As can be seen, present smooth wall skin-friction coefficients are in reasonable agreement with the findings of previous investigators and with the correlation/calculation scheme of Spalding-Chi[42] (within ~20% of the latter, as calculated for a nominal Mach number of 3; data and calculations are as reported by Sturek[43]). Some recent, unpublished data of Voisinet, obtained on the flat nozzle wall of the NOL Boundary Layer Channel, via a small floating element balance, are also shown.

A second, more pertinent, comparison is shown in Figure 12, wherein the rough-to-smooth wall skin-friction coefficient ratio is plotted as a function of the logarithm of roughness Reynolds number. These correlating parameters were originally proposed by Nikuradse[8] (incompressible flow) and Goddard[9] (compressible flow) and were based on their sand-grain results. The present data plus those V-groove roughness results of Young[18], Mann[20], and Wade[11], are shown in comparison with the bounds of Goddard's[9] compressible, sand-grain results (note that all

data shown are for adiabatic flow). Several key points are mentioned in the succeeding paragraphs.

1. Present sand-grain results resubstantiate Goddard's[9] correlation and the conclusion emanating from it, namely that "the effect of surface roughness on skin-friction drag is localized deep within the boundary layer at the surface itself and is independent of the external flow, i.e., Mach number, per se, is eliminated as a variable." The significance of the breaking point in the correlation, $(C_f/C_{f_o}) > 1$ for $Re_k > 10$ or 11, has been discussed earlier in this section (Eqs. (12)).

2. A similar functional dependence between (C_f/C_{f_o}) and Re_k has also been demonstrated for machined (V-groove) roughnesses, as superimposed on both flat and single periodic waveform surfaces, via present data and previously published results. For these type surfaces, equivalent sand-grain roughnesses must not differ substantially from actual roughness dimensions, considering the observed level of agreement with the bounds of Goddard's sand-grain results.

3. Superposition of roughness on surfaces which simultaneously possessed both short and long periodic waveforms (models 10, 11, 12) resulted in a narrow, self-consistent band of data, but one which failed to fall within the bounds of Goddard's correlation. Rather, these results (plotted using k, not ε_{SW}, as the roughness scale in Re_k), departed from the $(C_f/C_{f_o}) = 1.0$ line at Re_k values near 4 to 5, and thereafter exhibited a functional dependence on Re_k similar to that of the original correlation. Such behavior is indicative of the amplification in surface shear stress caused by this type of rough/multiple waveform surface. Increases in surface shear,

above smooth wall levels, were observed for these cases even though the superimposed roughness scale, k, would not have been sufficient, by itself, to cause such increases, i.e., at the departure from the $(C_f/C_{f_o}) = 1.0$ line the roughness dimension of each rough/multiple waveform surface was always less than one-half the corresponding sublayer thickness.

4. The motor case (i.e., random rough/wavy wall) data, plotted using its ascribed k value, did not correlate with any of the other results. A horizontal shift applied to these data via a replacement of the k roughness scale in Re_k with ε_{SW} (ascribed short-wave amplitude) brought them within the bounds of other results, but the weaker functional dependence on roughness Reynolds number remained, of course, unchanged, i.e., the slope of (C_f/C_{f_o}) versus Re_k remained below that possessed by other results.

C. Smooth and Rough Wall Temperature Profiles

Limited temperature profile data were obtained for smooth wall and #24 grit rough wall conditions. These data were needed to verify certain temperature-velocity relationships frequently assumed in compressible, adiabatic flow data reduction. This section summarizes those results.

The generalized total temperature-velocity relationship of Danberg[44] can be written,

$$\bar{T} = \beta\bar{u} + (1 - \beta)\bar{u}^2 \tag{13}$$

where,

$$\bar{T} = \left[\frac{T_o - T_w}{T_{o_\infty} - T_w}\right]$$

$$\bar{u} = (u/u_\infty)$$

$$\beta = \left[\frac{T_{aw} - T_w}{T_{o_\infty} - T_w}\right]$$

$$r = \left[\frac{T_{aw} - T_\infty}{T_{o_\infty} - T_\infty}\right] \qquad \text{(recovery factor)}$$

This generalized expression reduces to two well-known special cases. First, for unit Prandtl number, where r = 1.0

$$T_{aw} = T_{o_\infty} \quad ; \quad \beta = 1.0$$

and,

$$\bar{T} = \bar{u} \quad \text{(Crocco relation)} \tag{14}$$

Second, for adiabatic flow, where $r \neq 1.0$*,

$$T_w = T_{aw} \quad ; \quad \beta = 0$$

and,

$$\bar{T} = \bar{u}^2 \quad \text{(quadratic or Walz relation)} \tag{15}$$

Figure 13 presents smooth and #24 grit rough wall data in comparison with Equations (14) and (15). A total temperature overshoot, and agreement with the quadratic expression, were noted in each case, characteristic of adiabatic, nozzle wall boundary layers.

For use in actual profile data reduction, a static temperature-velocity relationship was desired. According to Walz[2], a generalized static temperature-velocity relationship can be written as,

$$\left(\frac{T}{T_\infty}\right) = A + B\left(\frac{u}{u_\infty}\right) + C\left(\frac{u}{u_\infty}\right)^2 \tag{16}$$

where coefficients are evaluated from the following boundary conditions:

(1) for $u = 0$, $T = T_w$

(2) for $u = u_\infty$, $T = T_\infty$

(3) for adiabatic flow, $T_w = T_{aw}$ and $\left(\frac{\partial T}{\partial y}\right)_w = 0$; thus,

---

* Simultaneous assumption of $r = 1.0$ and adiabatic flow would leave β undefined, i.e., $T_{aw} = T_{o_\infty} = T_w$ and $\beta = 0/0$.

$$\left(\frac{\partial T}{\partial y}\right)_w = 0 = \left(\frac{\partial T}{\partial u}\right)_w \cdot \left(\frac{\partial u}{\partial y}\right)_w$$

but, $\left(\frac{\partial u}{\partial y}\right)_w \neq 0$, therefore,

$$\left(\frac{\partial T}{\partial u}\right)_w = 0 \quad , \text{ where } u = 0$$

Thus:

$$A = \frac{T_w}{T_\infty}$$

$$B = \left[\frac{T_{aw} - T_w}{T_\infty}\right]$$

$$C = \left[1 - \frac{T_{aw}}{T_\infty}\right] \qquad (r \neq 1.0)$$

For adiabatic flow, where $\beta = 0 = B$, Equations (13) and (16) can be shown, mathematically, to be equivalent. Figures 14a-b show present results in comparison with Equation (16). As can be seen, the agreement is very good. Consequently, Equation (16) was used to reduce all profile data where actual temperature measurements were not made.

D. Smooth and Rough Wall Velocity Profiles

In order to effectively present and discuss velocity profile results, certain mathematical considerations for smooth and rough wall turbulent boundary layers must be reviewed.

Since we are dealing with compressible flow, a velocity transformation to the incompressible plane is required before any comparisons between present results and previously published mathematical formulations and/or experimental results can be undertaken. In this investigation, a transformation based on

the work of Van Driest[45] was used[†]:

$$u^* = \left(\frac{u_\infty}{A}\right)\left[\sin^{-1}\left(\frac{2A^2\,\frac{u}{u_\infty} - B}{\sqrt{B^2 + 4A^2}}\right) + \sin^{-1}\left(\frac{B}{\sqrt{B^2 + 4A^2}}\right)\right] \tag{17}$$

where,

$$A = \sqrt{\frac{T_{aw} - T_\infty}{T_w}} = \sqrt{\left(\frac{T_\infty}{T_w}\right) r\left(\frac{\gamma - 1}{2}\right) M_\infty^2}$$

$$B = \left[\frac{T_{aw}}{T_w} - 1\right]$$

r = recovery factor $\neq 1.0$

Velocities appearing in all subsequent correlation schemes (i.e., $[u^+, y^+]$, $[(u - u_\infty)/u_\tau, (y/\delta)]$ and $[(\Delta u/u_\tau), Re_k]$ coordinates) are transformed values; continued use of the * superscript will not be made.

An excellent review of smooth and rough wall turbulent boundary-layer correlation techniques was given by Clauser[3]; a brief summary follows.

Within the turbulent boundary layer three distinct regions have been found to exist:

1. an inner, or viscous sublayer region, where

$$(u/u_\tau) = g\left(\frac{y u_\tau}{\nu_w}\right) \quad ; \tag{18}$$

2. an outer, or velocity defect region (sometimes referred to as the wake region), where

$$\left[\frac{u - u_\infty}{u_\tau}\right] = f\,(y/\delta) \quad ; \tag{19}$$

[†] As programmed in the NOL Law of the Wall - Law of the Wake data-reduction program; the assistance of Robert L. P. Voisinet in adapting this program for use in the present investigation is gratefully acknowledged.

3. an overlapping, or law-of-the-wall region.

In order to deduce a mathematical formulation for the overlapping region (Eq. (4) describes the sublayer), the following argument was presented: Within the overlapping region, both Equations (18) and (19) must hold; therefore, equating (u/u_τ) expressions,

$$f(y/\delta) + \left(\frac{u_\infty}{u_\tau}\right) = g\left(\frac{y}{\delta} \cdot \frac{\delta u_\tau}{\nu_w}\right) \tag{20}$$

A comparison of the two sides of Equation (20) shows that the effect of the multiplication factor $\left(\frac{\delta u_\tau}{\nu_w}\right)$ inside g must be equivalent to the additive term $\left(\frac{u_\infty}{u_\tau}\right)$ outside f; the logarithm is the only function with this property. Thus, within the overlapping region,

$$(u - u_\infty)/u_\tau = A \log_{10}(y/\delta) + B \tag{21}$$

$$\left.\begin{aligned} (u/u_\tau) &= A \log_{10}\left(\frac{yu_\tau}{\nu_w}\right) + C \\ u^+ &= A \log_{10}(y^+) + C \end{aligned}\right\} \tag{22}$$

Equation (22) defines the law-of-the-wall, in the absence of roughness effects. Equality of slopes for Equations (21) and (22), within their mutual regime of validity, can be demonstrated by equating (u/u_τ) expressions from each and differentiating both sides with respect to the nondimensional coordinate (y/δ). This requirement for equality of slopes within the law-of-the-wall region provides one self-consistency check on profile data.

Coles[4] has formulated an additive term for Equation (22) in order to generate a simultaneous mathematical expression for

both the law-of-the-wall and law-of-the-wake regions (i.e., for all y^+ values > 11). However, since primary emphasis here has been placed on roughness effects, and since roughness does not strongly influence the outer or wake region (as will be demonstrated in Fig. 17), no attempts have been made to compare present profile data with Coles' formulation (previous NOL studies[39], involving pressure gradient effects on smooth wall turbulent boundary-layer development, have included such analyses).

Roughness effects on the mean velocity profile are primarily concentrated in the inner 20 percent of the layer, i.e., within the viscous sublayer and law-of-the-wall (logarithmic) region. Effects of roughness on the law-of-the-wall have been reasoned, and verified experimentally, to be reflected solely as a shift in the intercept C of Equation (22). The shift, itself, is a function of the roughness Reynolds number, Re_k, i.e., for rough walls,

$$(u/u_\tau) = A \log_{10}\left(\frac{yu_\tau}{\nu_w}\right) + C - \left(\frac{\Delta u}{u_\tau}\right) \tag{23}$$

where,

$$A = \text{smooth wall } u^+, y^+ \text{ slope}$$

$$\left(\frac{\Delta u}{u_\tau}\right) = f(Re_k) \tag{24}$$

For large roughness Reynolds numbers (Re_k > ~70), the sublayer is destroyed and the inner regions of the boundary layer must become independent of viscosity. For these conditions to be met, Equation (24) must be of the form

$$\left(\frac{\Delta u}{u_\tau}\right) = A \log_{10}\left(\frac{ku_\tau}{\nu_w}\right) + D \qquad \text{[fully rough]} \tag{25}$$

which can be verified by substituting Equation (25) into Equation (23): the resulting, fully rough, expression

$$u^+ = A \log_{10}(y/k) + C - D \qquad \text{[fully rough]} \tag{26}$$

shows no viscosity dependence.

The fact that the slope of $(\Delta u/u_\tau)$ versus $\log_{10}(Re_k)$, for $Re_k > \sim 70$, must match the smooth wall u^+, y^+ slope, provides another self-consistency check on profile data.

A technique originated by Clauser[46] provides still another self-consistency check between measured shear and profile data. Here the surface shear stress is inferred from the velocity profile slope. Eliminating τ_w from the definitions of u_τ and C_f results in

$$u_\tau = \sqrt{\frac{C_f}{2} \frac{\rho_\infty}{\rho_w}}\; u_\infty \tag{27}$$

Substituting Equation (27) into Equation (23) and rearranging yields,

$$\left(\frac{u}{u_\infty}\right) = A\sqrt{\frac{C_f}{2} \frac{\rho_\infty}{\rho_w}}\; \log_{10}(y) + \text{[terms with no y dependence]} \tag{28}$$

This technique then calls for plotting (u/u_∞) versus $\log_{10}(y)$ and measuring the slope, S, in the logarithmic region. From Equation (28)

$$S = A\sqrt{\frac{C_f}{2} \frac{\rho_\infty}{\rho_w}} \tag{29}$$

or,

$$C_f = 2\,\frac{S^2}{A^2} \cdot \frac{\rho_w}{\rho_\infty} \tag{30}$$

Inferred skin-friction coefficients were obtained in this manner for two limiting cases and the results are shown below:

	$C_{f_{meas.}}$	$C_{f_{infer.}}$	$\frac{\Delta C_f}{C_{f_{meas.}}}$
smooth wall, (1 atm) :	1.81×10^{-3}	1.69×10^{-3}	-0.066
fully rough wall, (#24 grit, 2 atm.) :	3.51×10^{-3}	3.17×10^{-3}	-0.097

Levels of agreement, within measurement accuracy, were noted.

In order to conduct any such analysis of rough wall profile data, the question of effective y origin must be addressed. Figure 15 schematically depicts this problem. Actual Pitot probe measurements can only be made down to the roughness peaks, i.e., to the point of probe contact. However, previous investigators (e.g., Scottron[13] and Perry[14]) have found that the effective y origin lies somewhere between the roughness peaks and valleys.

Systematic variations were therefore applied to the y origin, such that

$$y' \text{ (shifted origin)} = y \text{ (probe origin)} + ak$$

where,

$$a = 0,\ 1/2,\ 1$$

$$k = k,\ \varepsilon^*_{SW},\ \varepsilon^*_{LW}$$

and corresponding velocity profiles were plotted in both $[u^+, y^+]$ and $[(u - u_\infty)/u_\tau,\ (y/\delta)]$ coordinates, e.g., Figure 16. An effective y origin was thereby defined by that particular shift $(a \cdot k)$ which brought the rough wall velocity profile data parallel

*Models 7 through 12, where appropriate.

to the smooth wall u^+, y^+ slope, within the logarithmic region (recall Eq. (23)). Examination of all such plots showed that the combination of $a = 1/2$, $k = k$, most consistently met this criterion, even for the rough/wavy wall cases (evidently, those larger shifts associated with waveform amplitudes were unrealistic). The #24 grit, 1 atm., profile data were selected for presentation in Figure 16 because they most clearly illustrate the features discussed above.

An effective y origin, determined in this manner, is utilized in all subsequent profile plots. Note that the continued use of the prime superscript on y will not be made.

Figure 17 shows present profile data, in terms of velocity defect coordinates, in comparison with the range of smooth and rough wall incompressible results reported by Clauser[3]. The level of agreement is seen to be quite good. Several points concerning this figure should be made.

1. All smooth and rough wall data collapse to a nearly universal curve in the outer 80 percent of the layer (i.e., in the wake region, $(y/\delta) > \sim 0.2$), showing that the effects of roughness are indeed localized deep within the boundary layer.

2. As one views data below the wake region (inner 20 percent of the layer), some variation between smooth and rough wall results becomes apparent. With the exception of the random rough/wavy (molded surface) data, all rough wall data are displaced slightly downward (in these coordinates) from the smooth wall curve. Similar observations have been made elsewhere[47].

3. All smooth and rough wall data, within the logarithmic region, possess slopes which match the smooth wall u^+,y^+ slope, thereby demonstrating a self-consistency check noted earlier.

Figures 18a-c show present profile data plotted in terms of u^+,y^+ coordinates. Data are subdivided into three groups, as was done in Figure 9, for ease in interpretation. As before, the smooth wall results are shown on each plot for reference purposes.

Figure 18a shows smooth and sand-grain results. These data cover the entire range of possible roughness regimes, from aerodynamically smooth to fully rough. The curved solid line represents the theoretical sublayer velocity distribution ($u^+ = y^+$). The straight solid line through the smooth wall data is described by Equation (22), i.e., the law-of-the-wall correlation. Present smooth wall slope and intercept were found to be 4.33 and 5.50 (at 1 atm.), respectively. Under the influence of roughness, velocity profiles were seen to shift downward, to the right, from the smooth wall curve, while remaining parallel to it within the logarithmic region (all straight solid lines are parallel). Such observations resubstantiate the discussions centered around Equation (23).

Less notable velocity shifts (if any) were observed for the molded and machined surfaces, due primarily to conditions at which measurements were made (i.e., at 1 atm. total pressure, where most C_f values for these models were found to approximate the smooth wall level). However, results shown in Figures 18b-c

lend themselves to an important conclusion, namely, that velocity profiles over rough/wavy surfaces (including random rough/wavy and rough/multiple periodic waveform surfaces) possess logarithmic regions wherein the law-of-the-wall correlation is valid.

Figure 19 concludes this section with a comparison between present and previously published data, showing roughness-induced velocity shift ($\Delta u/u_\tau$) as a function of Re_k. Observed velocity shifts for flows over sand-grain roughened surfaces were found to be in close agreement with other compressible and incompressible sand-grain results. Insufficient velocity shift data were obtained for flows over other surface conditions to warrant any meaningful comparisons and/or statements.

V CONCLUSIONS

Based on present results, their demonstrated levels of self-consistency, and favorable comparisons with previously published results, the following conclusions are stated:

1. Superposition of a given roughness dimension on a surface which simultaneously possessed both short and long (shallow) periodic waveforms increased surface shear above levels measured for identically rough surfaces possessing only one, or none, of these same periodic waveforms.

2. Equivalent sand-grain roughnesses for the random rough/wavy wall (motor case material) were of the order of four to eight times the physical roughness scale attributed to it.

3. Goddard's compressible skin-friction correlation, $(C_f/C_{f_o}) = \text{constant } [\log_{10} Re_k] + \text{constant}$, for $Re_k > \sim 10$, has been resubstantiated for sand-grain roughnesses. A similar

functional dependence between these variables has also been demonstrated for machined (V-groove) roughness patterns, as applied to both flat and single periodic waveform surfaces. Skin-friction data obtained on rough surfaces possessing multiple periodic waveforms were self-consistent and exhibited a like-functional dependence on Re_k, but showed departure from the $(C_f/C_{f_o}) = 1.0$ line at lower Re_k values (~ 5 as opposed to ~ 10 for all other results).

4. Walz' temperature-velocity relationship, for adiabatic flow, was found to accurately describe measured temperature profiles over both smooth and rough surfaces.

5. Velocity profiles measured over rough/wavy surfaces, including random rough/wavy and rough/multiple periodic waveform surfaces, were found to possess logarithmic regions wherein the law-of-the-wall correlation was valid.

6. When plotted in terms of velocity defect coordinates, present smooth, rough, and rough/wavy profile data collapsed to a near universal curve in the outer portions of the layer, in agreement with previously published results, verifying that, even for the complex surface patterns considered here, roughness effects are localized deep within the boundary layer.

VI REFERENCES

(1) Schlichting, H., Boundary Layer Theory, McGraw-Hill Book Co., Inc., New York, copyright 1960 (Library of Congress #59-15472).

(2) Walz, A., Boundary Layers of Flow and Temperature, MIT Press, Cambridge, Mass., 1969 (Library of Congress #69-12761).

(3) Clauser, F. H., "The Turbulent Boundary Layer," Advances in Applied Mechanics, Vol. IV, 1956, pp. 1-51.

(4) Coles, D., "The Law of the Wake in the Turbulent Boundary Layer," J. Fluid Mechanics, Vol. 1, 1956, pp. 191-226.

(5) Kovasznay, L. S. G., "Structure of the Turbulent Boundary Layer," Physics of Fluids, Supplement on Boundary Layers and Turbulence, 1967, pp. S25-S30.

(6) Kline, S. J., Morkovin, M. V., Sovran, G., and Cockrell, D. J., editors, "Computation of Turbulent Boundary Layers - 1968 AFOSR-IFP-Stanford Conference. Vol. I - Methods, Predictions, Evaluation and Flow Structure," Stanford University, c.1969.

(7) Bertram, M. H., editor, "Compressible Turbulent Boundary Layers," NASA SP-216, Dec. 1968.

(8) Nikuradse, J., "Laws of Flow in Rough Pipes," English translation, NACA TM No. 1292, Nov. 1950.

(9) Goddard, F. E., Jr., "Effect of Uniformly Distributed Roughness on Turbulent Skin-Friction Drag at Supersonic Speeds," J. Aero/Space Sciences, Vol. 26, No. 1, Jan. 1959, pp. 1-15, 24.

(10) Hama, F. R., "Boundary Layer Characteristics for Smooth and Rough Surfaces," Transactions Society Naval Architects Marine Engineers, Vol. 62, 1954, pp. 333-358.

(11) Wade, J. H. T., "An Experimental Investigation of the Effect of Surface Roughness on the Drag of a Cone-Cylinder Model at a Mach Number of 2.48," University of Toronto Inst. for Aerophysics Report No. 34, Sept. 1955 (N65-86882).

(12) Perry, A. E., and Joubert, P. N., "Rough-Wall Boundary Layers in Adverse Pressure Gradients," J. Fluid Mechanics, Vol. 17, 1963, pp. 193-211.

(13) Scottron, V. E., "Turbulent Boundary Layer Characteristics over a Rough Surface in an Adverse Pressure Gradient," D. Eng. Thesis, Johns Hopkins University, 1967 (Univ. Microfilms #68-6577).

(14) Perry, A. E., Schofield, W. H., and Joubert, P. N., "Rough Wall Turbulent Boundary Layers," J. Fluid Mechanics, Vol. 37, Part 2, 1969, pp. 383-413.

(15) Simpson, R. L., "A Generalized Correlation of Roughness Density Effects on the Turbulent Boundary Layer," AIAA J., Vol. 11, No. 2, Feb. 1973, pp. 242-244.

(16) Owen, P. R., and Thomson, W. R., "Heat Transfer across Rough Surfaces," J. Fluid Mechanics, Vol. 15, 1963, pp. 321-334.

(17) Dipprey, D. F., and Sabersky, R. H., "Heat and Momentum Transfer in Smooth and Rough Tubes at Various Prandtl Numbers," International J. Heat and Mass Transfer, Vol. 6, No. 5, May 1963, pp. 329-353.

(18) Young, F. L., "Experimental Investigation of the Effects of Surface Roughness on Compressible Turbulent Boundary Layer Skin Friction and Heat Transfer," Univ. of Texas at Austin, Defense Research Laboratory Report DRL-532, May 1965 (AD 621-085).

(19) Young, F. L., and Westkaemper, J. C., "Experimentally Determined Reynolds Analogy Factors for Flat Plates," AIAA J., Vol. 3, No. 6, June 1965, pp. 1201-1202.

(20) Mann, H. W., "Experimental Study of the Compressible Turbulent Boundary Layer Skin Friction and Heat Transfer in the Fully Rough Regime," Univ. of Texas at Austin, Defense Research Laboratory Report DRL-554, Aug. 1967 (AD 822-169).

(21) Monta, W. J., Czarnecki, K. R., and Deveikis, W. D., "Drag Due to Two-Dimensional Surface Roughness in a Turbulent Boundary Layer at Mach 3 with and without Heat Transfer," NASA TN D-4746, Sept. 1968.

(22) Donne, M. D., and Meerwald, E., "Heat Transfer from Surface Roughened by Thread-Type Ribs at High Temperature," Proc. of 1970 Heat Transfer and Fluid Mechanics Institute, June 1970, pp. 354-370.

(23) Welsh, W. E., Jr., "Shape and Surface Roughness Effects on Turbulent Nosetip Ablation," AIAA J., Vol. 8, No. 11, Nov. 1970, pp. 1983-1989.

(24) Chin, J. H., "Effects of Surface Roughness on Heat Transfer to Ablating Bodies," AIAA J. Spacecraft and Rockets, Vol. 8, No. 7, July 1971, pp. 804-806.

(25) Powars, C. A., "Surface Roughness Effects on Reentry Heating," Aerotherm Tech. Memo TM-71-10, July, 1971.

(26) Nestler, D. E., "Compressible Turbulent Boundary-Layer Heat Transfer to Rough Surfaces," AIAA J., Vol. 9, No. 9, Sept. 1971, pp. 1799-1803.

(27) Chen, K. K., "Compressible Turbulent Boundary-Layer Heat Transfer to Rough Surfaces in Pressure Gradient," AIAA J., Vol. 10, No. 5, May 1972, pp. 623-629.

(28) Dvorak, F. A., "Calculation of Compressible Turbulent Boundary Layers with Roughness and Heat Transfer," AIAA J., Vol. 10, No. 11, Nov. 1972, pp. 1447-1451.

(29) Dirling, R. B., Jr., "A Method for Computing Roughwall Heat Transfer Rates on Reentry Nosetips," AIAA Paper No. 73-763, 8th Thermophysics Conf., July 1973.

(30) Smith, K. G., "The Increase in Wave Drag at Supersonic Speeds Due to Surface Waviness," RAE TR No. 65173, Aug. 1965.

(31) Kendall, J. M., "The Turbulent Boundary Layer over a Wall with Progressive Surface Waves," J. Fluid Mechanics, Vol. 41, Part 2, 1970, pp. 259-281.

(32) Czarnecki, K. R., and Jackson, M. W., "Theoretical Pressure Distributions over Arbitrarily Shaped Periodic Waves in Subsonic Compressible Flow and Comparison with Experiment," NASA TN D-5984, Nov. 1970.

(33) Muhlstein, L., Jr., "Experimental Investigation of the Influence of the Turbulent Boundary Layer on the Pressure Distribution over a Rigid Two-Dimensional Wavy Wall," NASA TN D-6477, Aug. 1971.

(34) Inger, G. R., and Williams, E. P., "Subsonic and Supersonic Boundary-Layer Flow Past a Wavy Wall," AIAA J., Vol. 10, No. 5, May 1972, pp. 636-642.

(35) Beebe, P. S., and Cermak, J. E., "Turbulent Flow over a Wavy Boundary," Proj. Themis TR No. 16, Colorado State University, May, 1972.

(36) Lee, R. E., et al., "The NOL Boundary Layer Channel," NOLTR 66-185, Nov. 1966.

(37) Voisinet, R. L. P. and Lee, R. E., "Measurements of a Mach 4.9 Zero Pressure Gradient Turbulent Boundary Layer with Heat Transfer, Part I - Data Compilation," NOLTR 72-232, Sep. 1972.

(38) Voisinet, R. L. P. and Lee, R. E., "Measurements of a Supersonic Favorable-Pressure-Gradient Turbulent Boundary Layer with Heat Transfer, Part I - Data Compilation," NOLTR 73-224, 1973.

(39) Voisinet, R. L. P., Lee, R. E., and Yanta, W. J., "An Experimental Study of the Compressible Turbulent Boundary Layer with an Adverse Pressure Gradient," AGARD Conference on Turbulent Shear Flows, AGARD CP No. 93, Sep. 1971.

(40) Danberg, J. E., "The Equilibrium Temperature Probe, A Device for Measuring Temperatures in Hypersonic Boundary Layers," NOLTR 61-2, Dec. 1961.

(41) O'Donnell, F. B., and Westkaemper, J. C., "Measurements of Errors Caused by Misalignment of Floating-Element Skin-Friction Balances," AIAA J., Vol. 3, No. 1, Jan. 1965, pp. 163-165.

(42) Spalding, D. B., and Chi, S. W., "The Drag of a Compressible Turbulent Boundary Layer on a Smooth Flat Plate with and without Heat Transfer," J. Fluid Mechanics, Vol. 18, Part I, Jan. 1964, pp. 117-143.

(43) Sturek, W. B., "An Experimental Investigation of the Supersonic Turbulent Boundary Layer in a Moderate Adverse Pressure Gradient, Part II. Analysis of the Experimental Data," Ballistic Research Laboratories Report BRL-1543, Jun. 1971 (AD 729-325).

(44) Danberg, J. E., "Characteristics of the Turbulent Boundary Layer with Heat and Mass Transfer at M = 6.7," NOLTR 64-99, Oct. 1964.

(45) Van Driest, E. R., "Turbulent Boundary Layer in Compressible Fluids," J. Aeronautical Sciences, Vol. 18, No. 3, March 1951, pp. 145-160, 216.

(46) Clauser, F. H., "Turbulent Boundary Layers in Adverse Pressure Gradients," J. Aeronautical Sciences, Vol. 21, No. 2, Feb. 1954, pp. 91-108.

(47) Furuya, Y., and Fujita, H., "Effect of Surface Roughness on the Velocity Defect Law," Physics of Fluids, Supplement on Boundary Layers and Turbulence, 1967, pp. S155-S156.

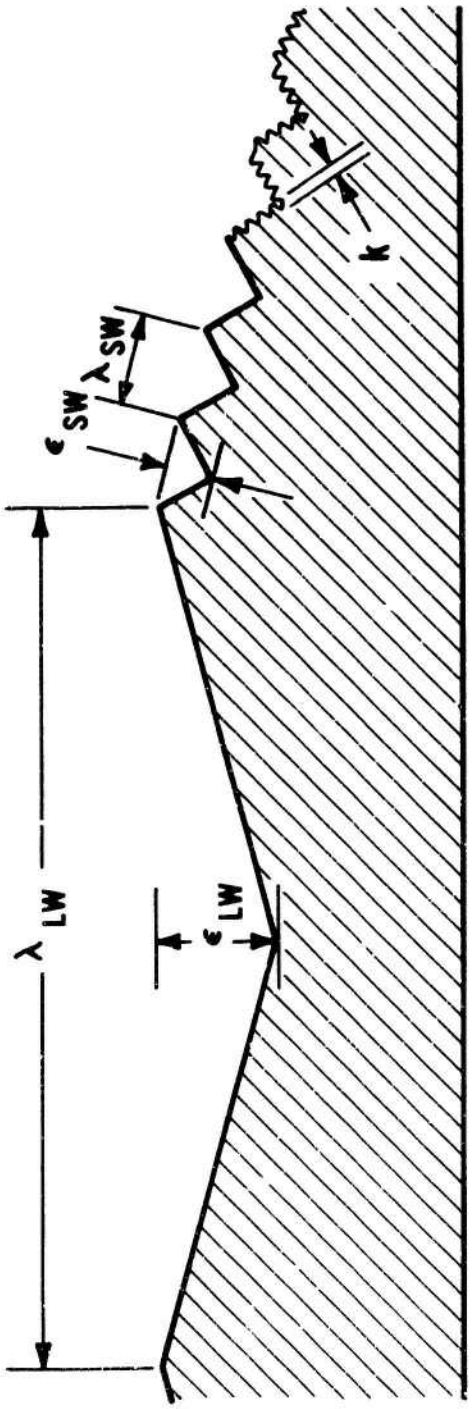

FIG. 1 MODEL SURFACE SCHEMATIC

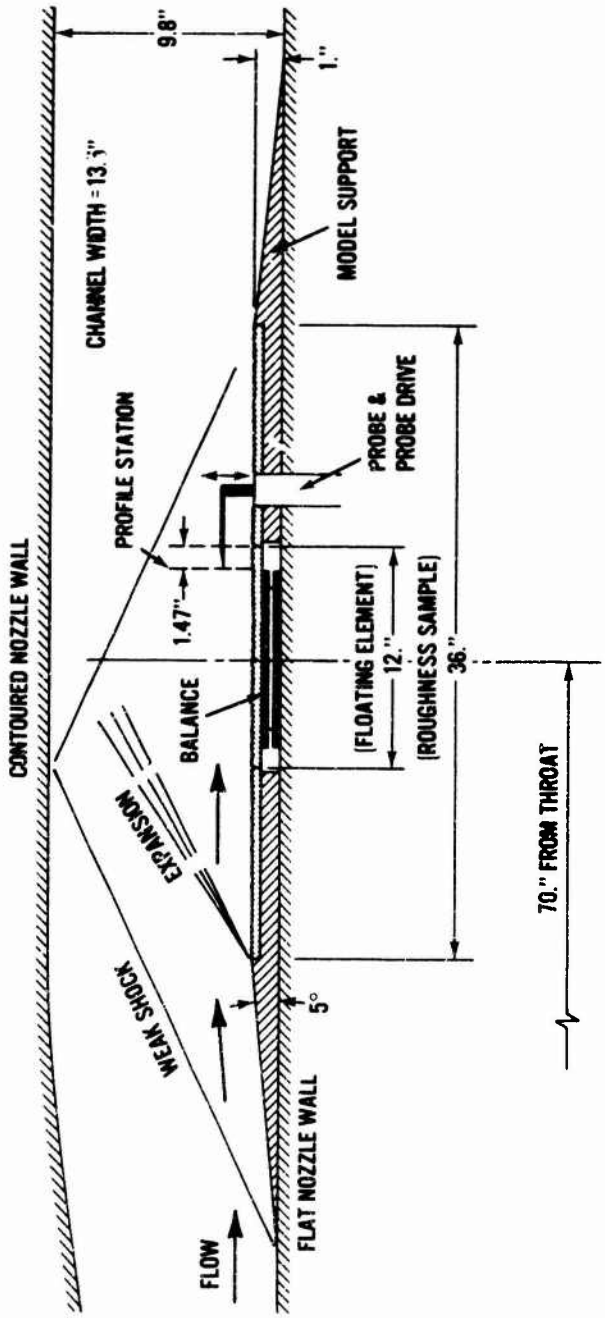

NOT TO SCALE

FIG. 2 TEST SETUP SCHEMATIC

FIG. 3 PHOTOGRAPH OF FLOATING ELEMENT, WITH CALIBRATION WEIGHT APPLIED, AND PITOT PROBE INSTALLED

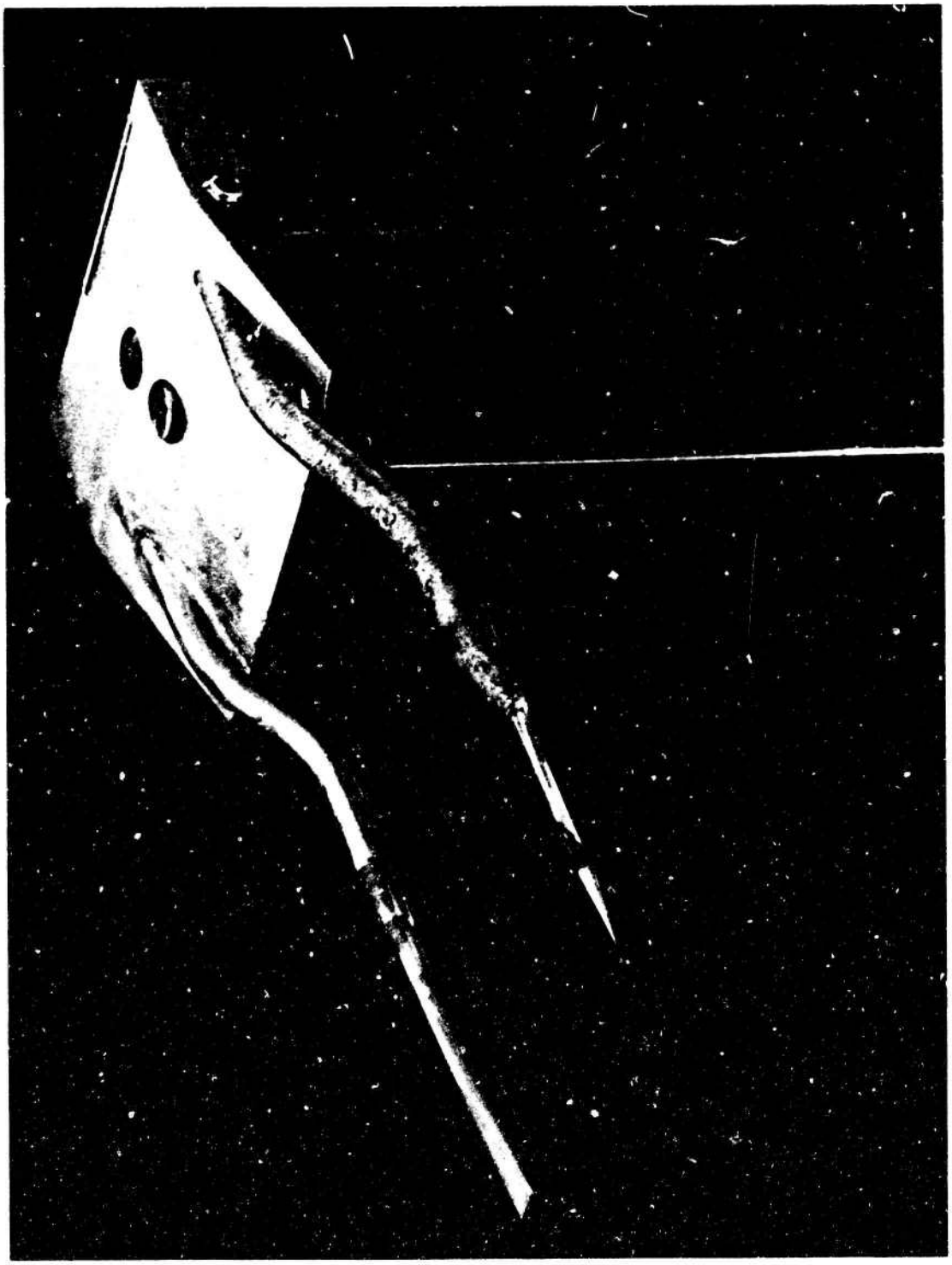

FIG. 4 PHOTOGRAPH OF DUAL PITOT RECOVERY TEMPERATURE PROBE

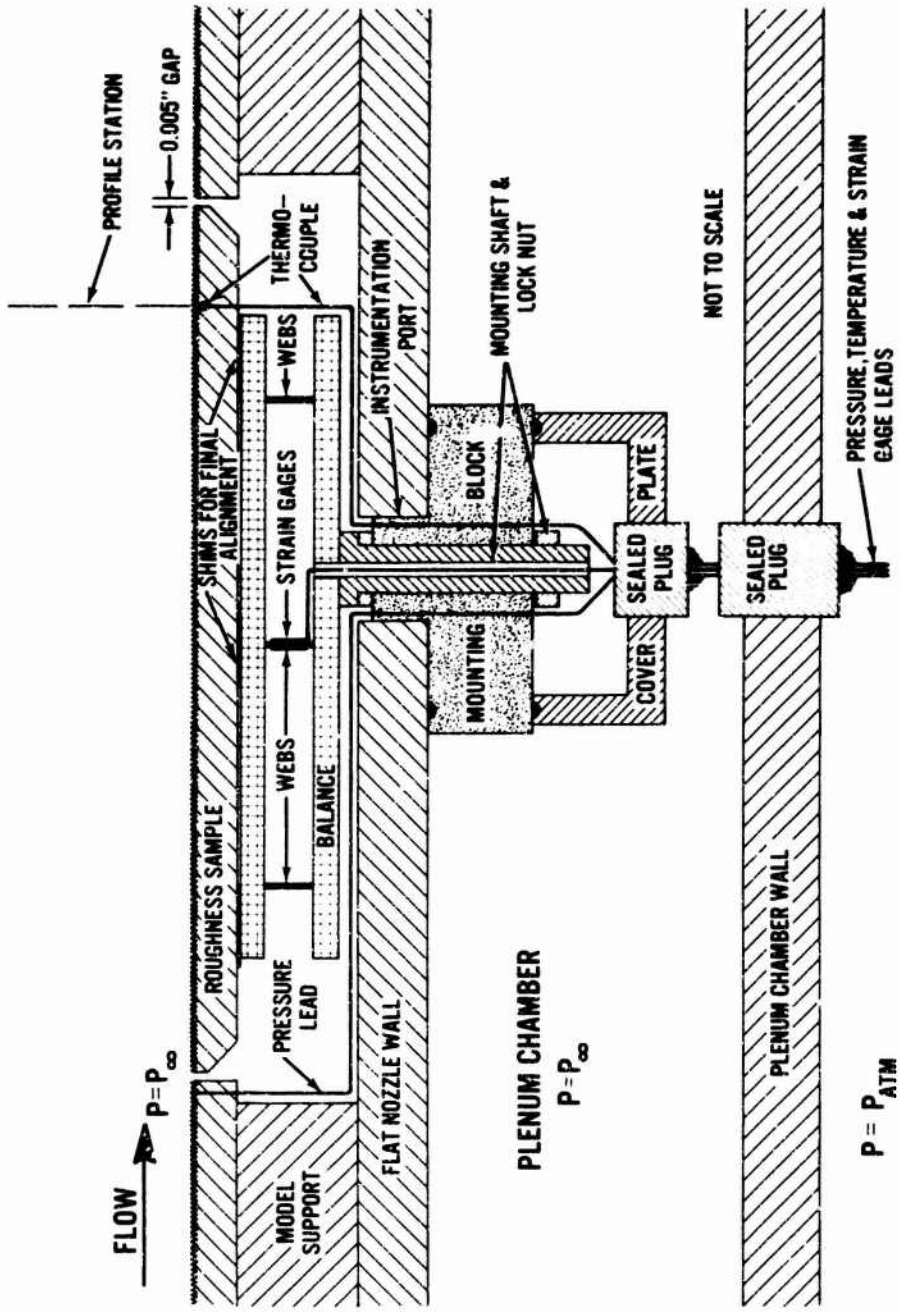

FIG. 5 SKIN-FRICTION BALANCE SCHEMATIC

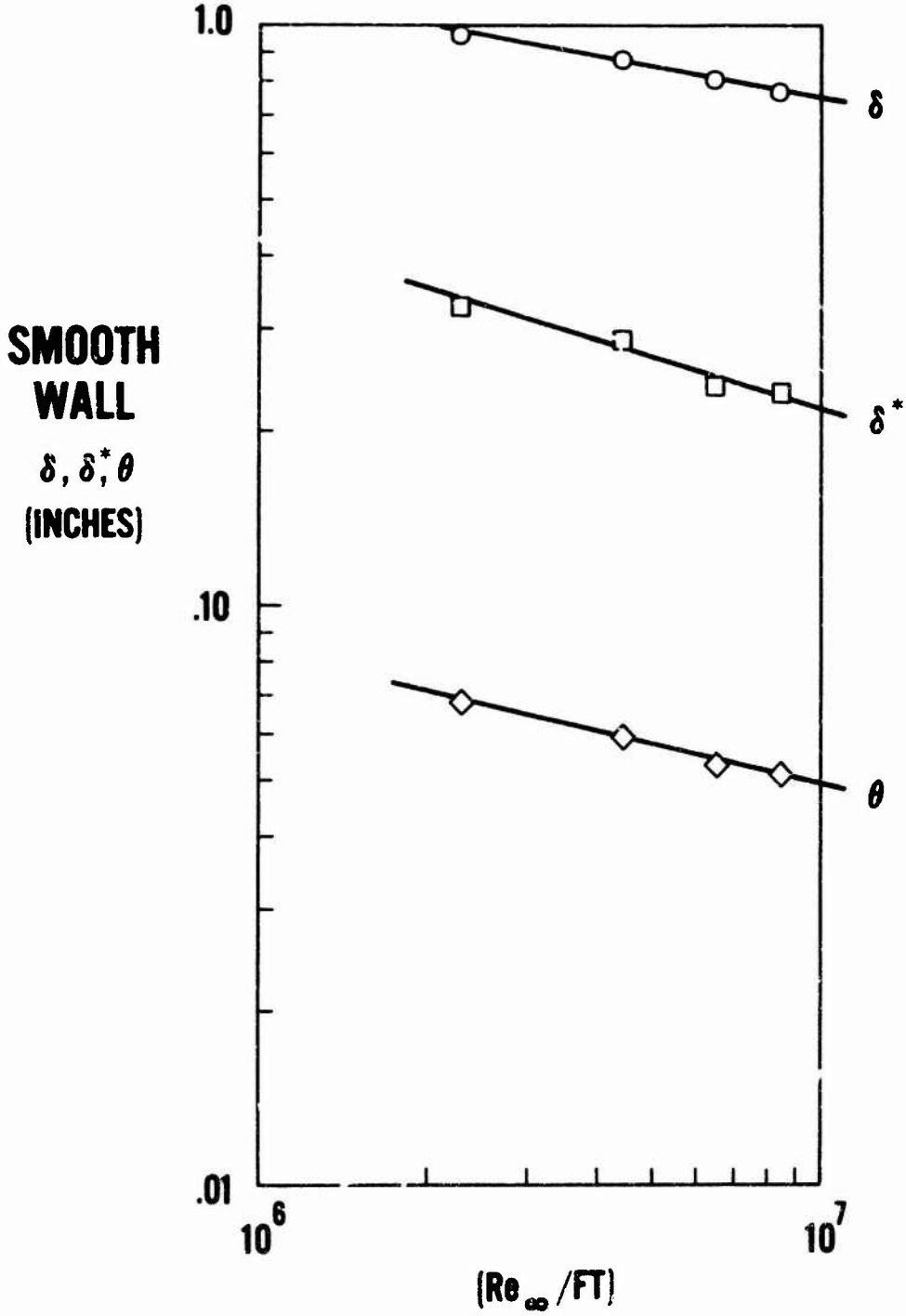

FIG. 6 SMOOTH WALL BOUNDARY LAYER CHARACTERISTICS

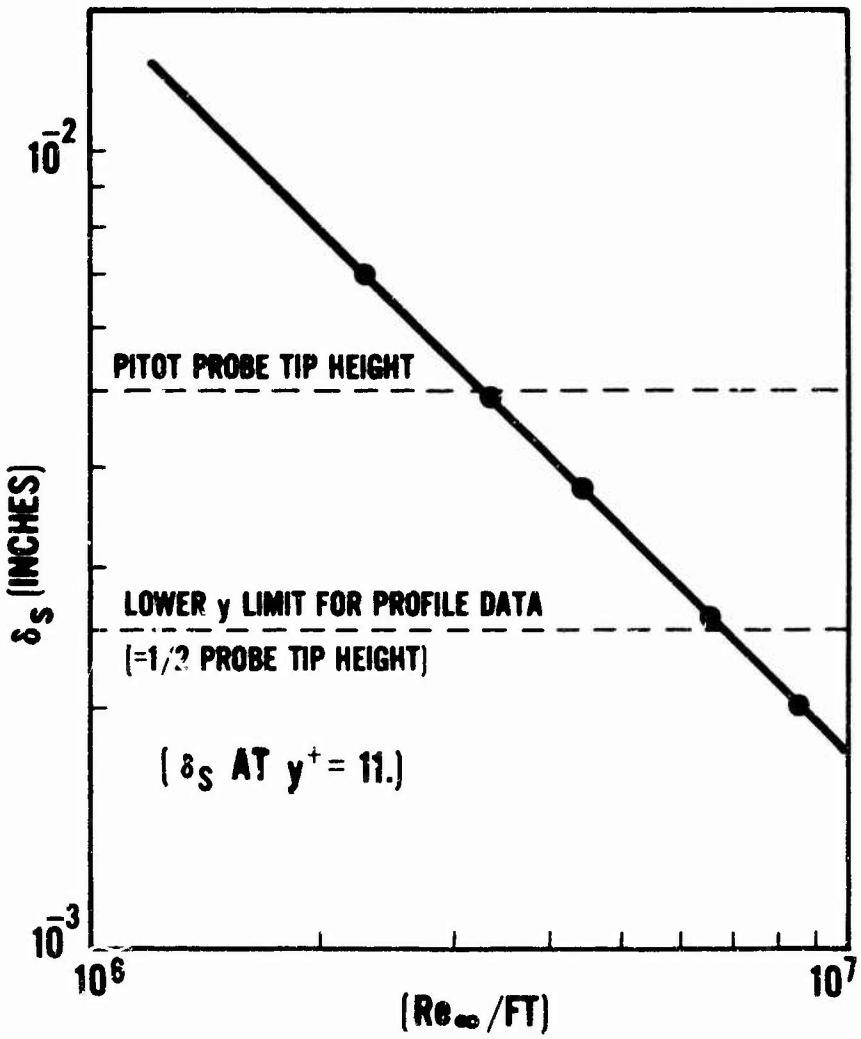

FIG. 7 SMOOTH WALL SUBLAYER THICKNESSES FROM MEASURED SHEAR

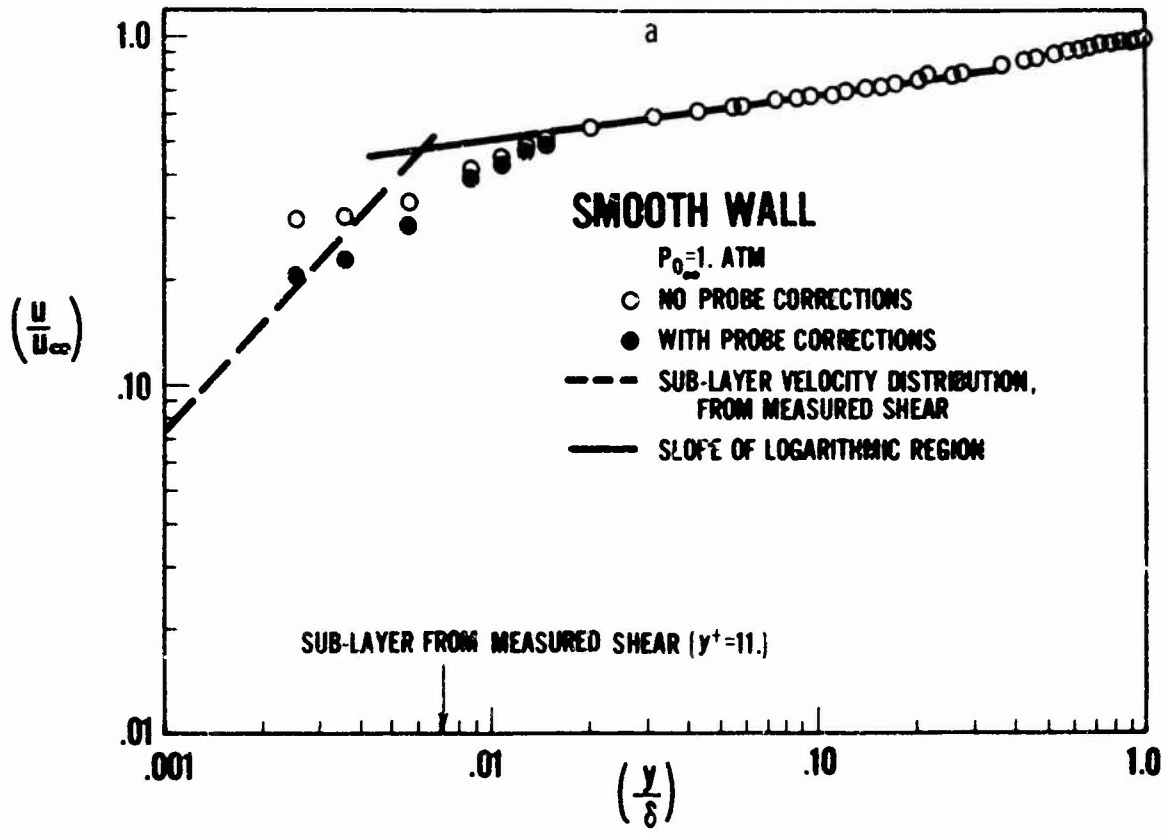

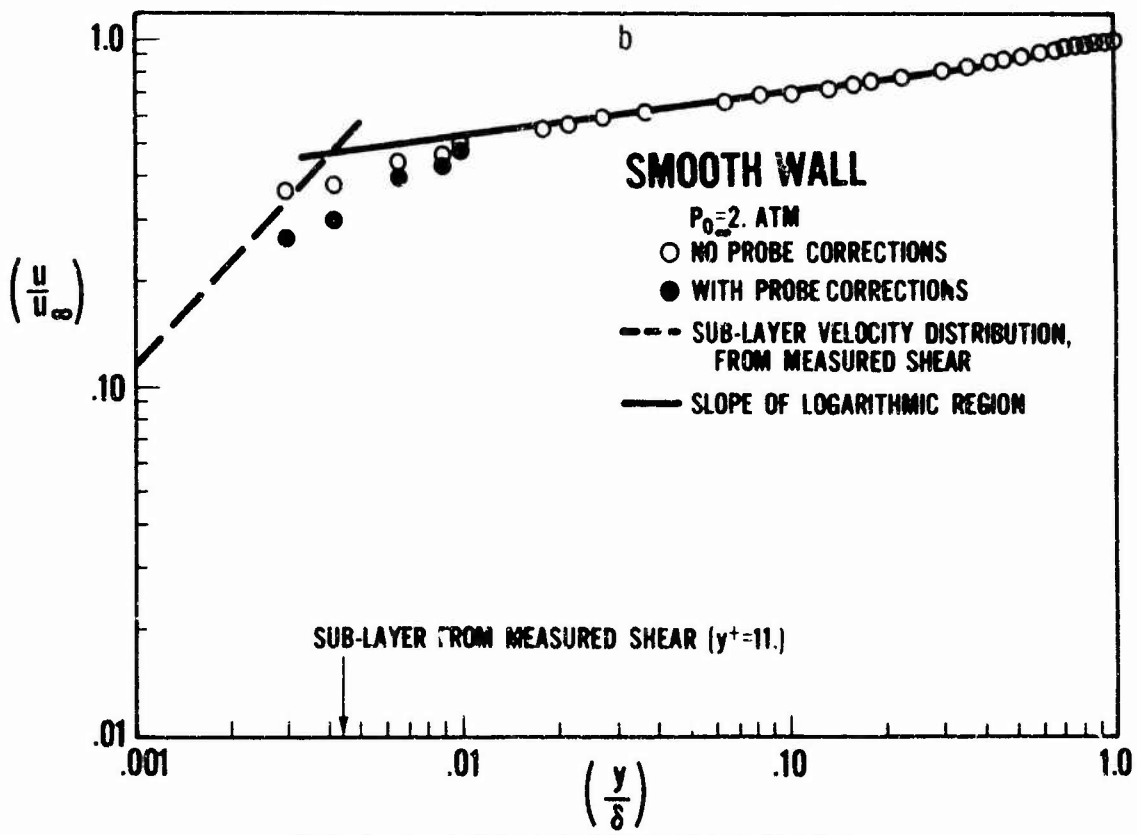

FIG. 8,a-b SMOOTH WALL VELOCITY PROFILES

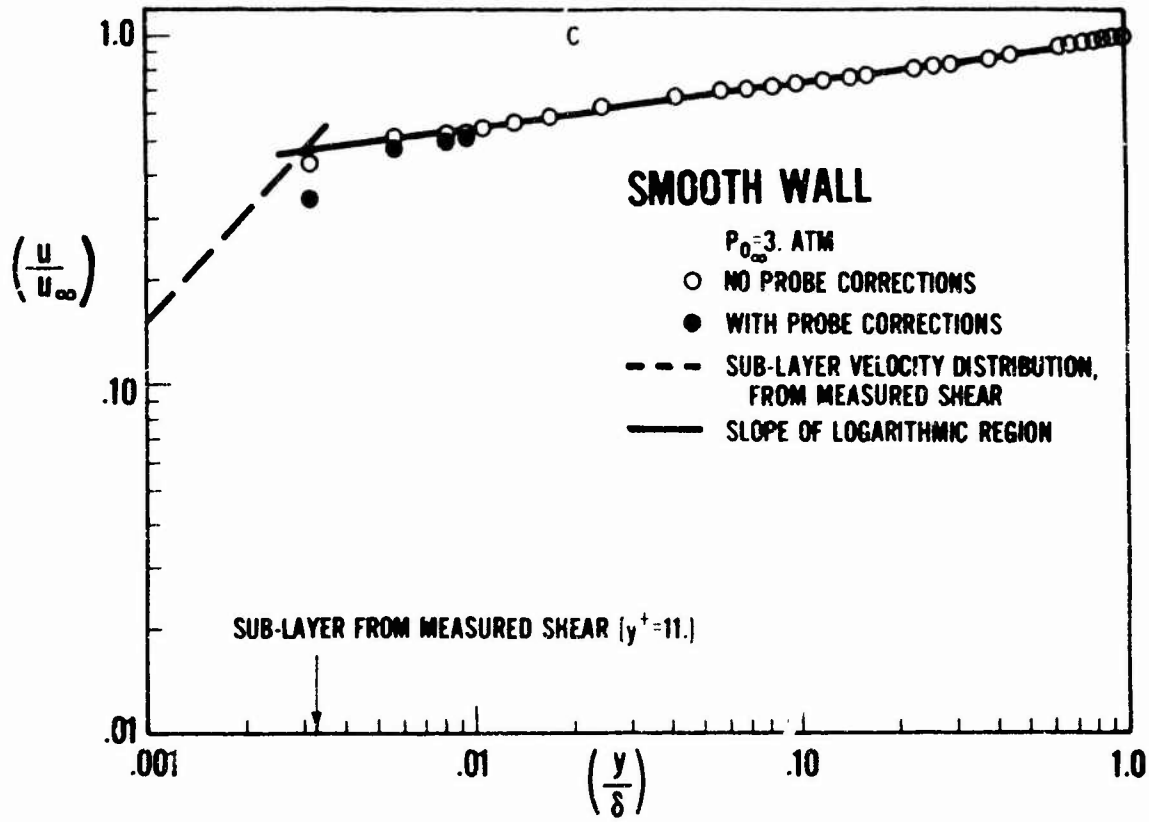

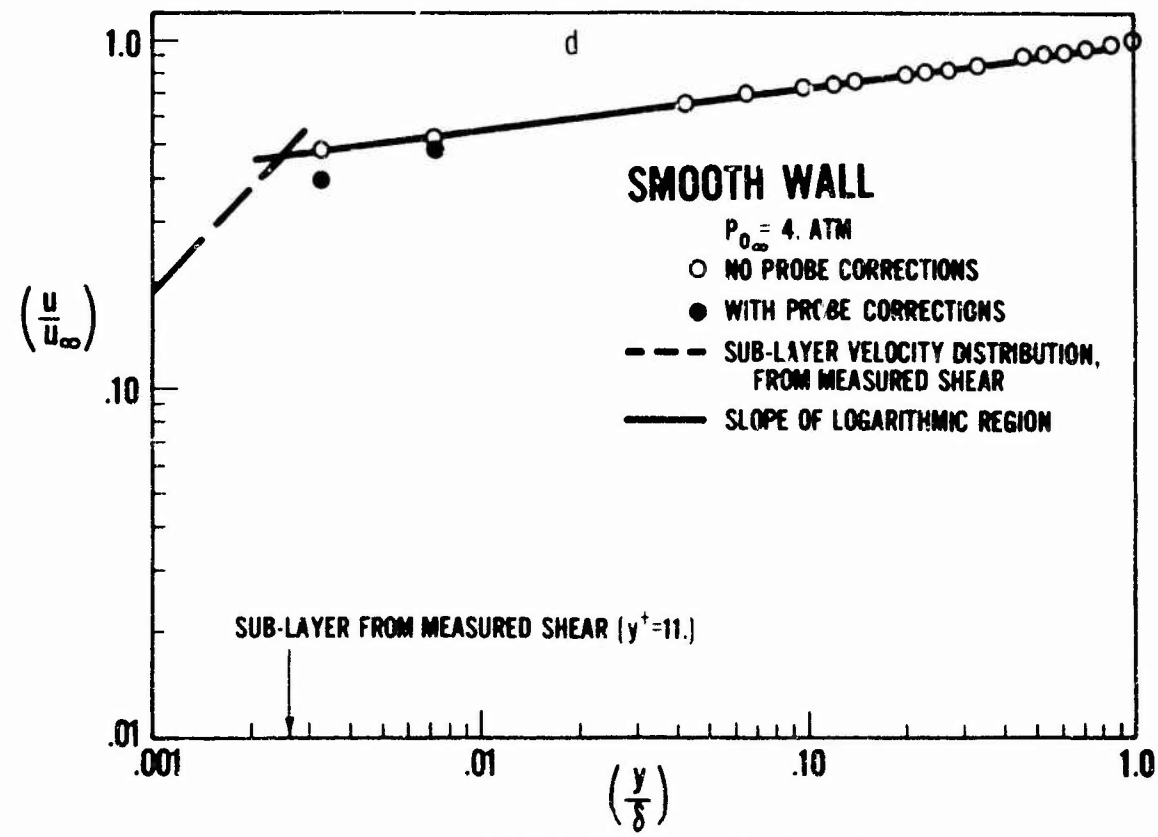

FIG. 8, c-d SMOOTH WALL VELOCITY PROFILES

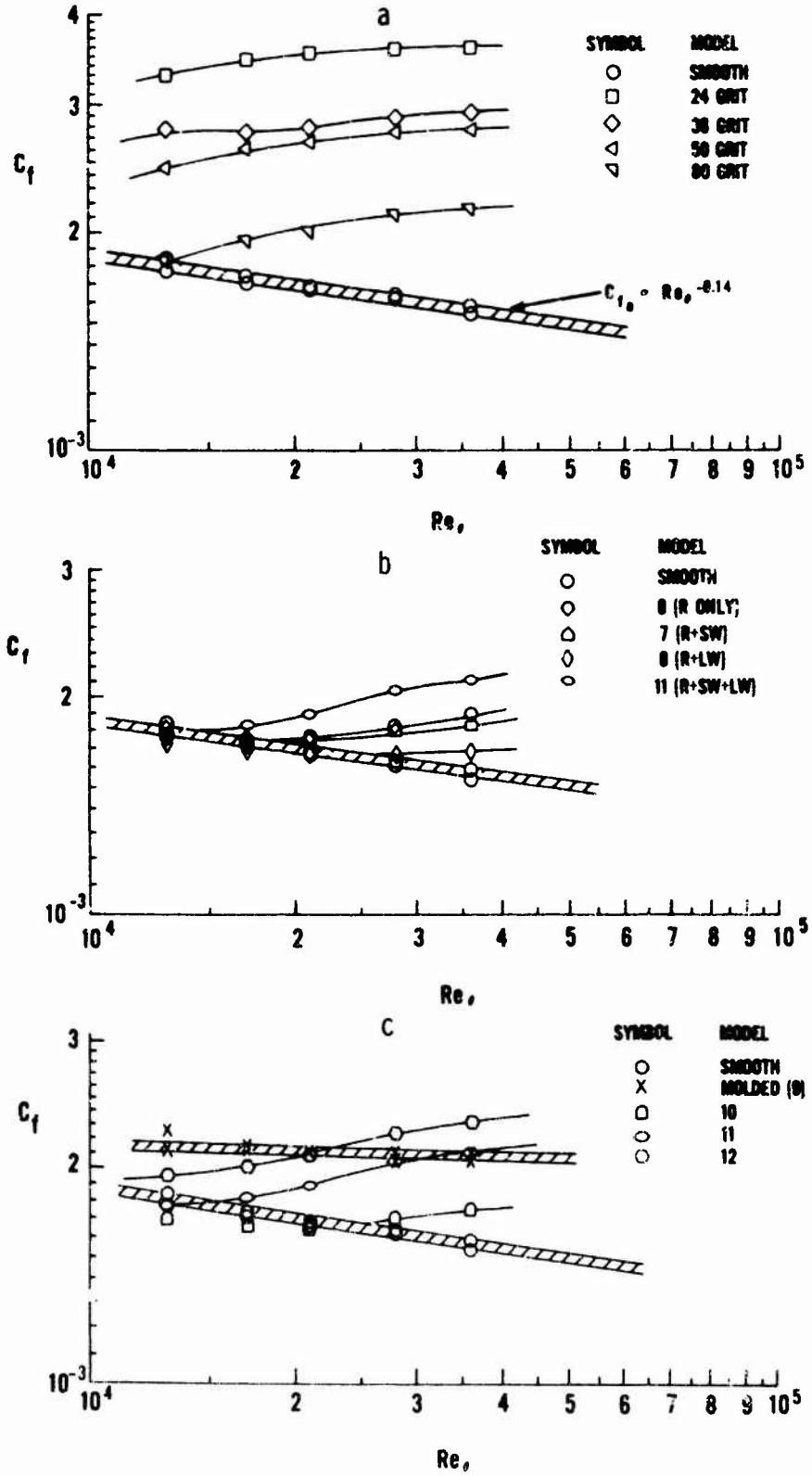

FIG. 9,a-b-c SMOOTH AND ROUGH WALL SKIN FRICTION COEFFICIENTS

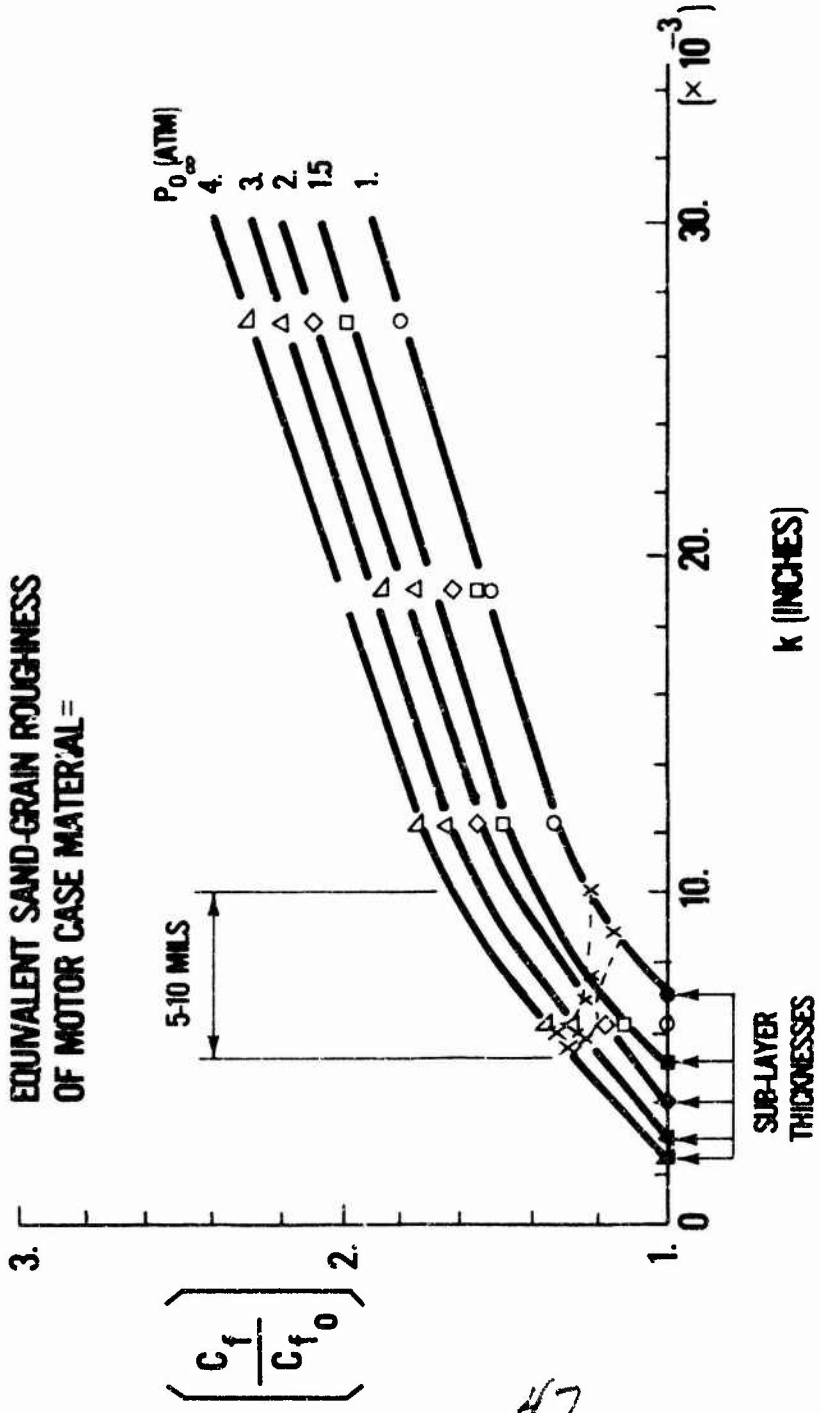

FIG. 10 EQUIVALENT SAND GRAIN ROUGHNESS DETERMINATION FOR MOTOR CASE MATERIAL

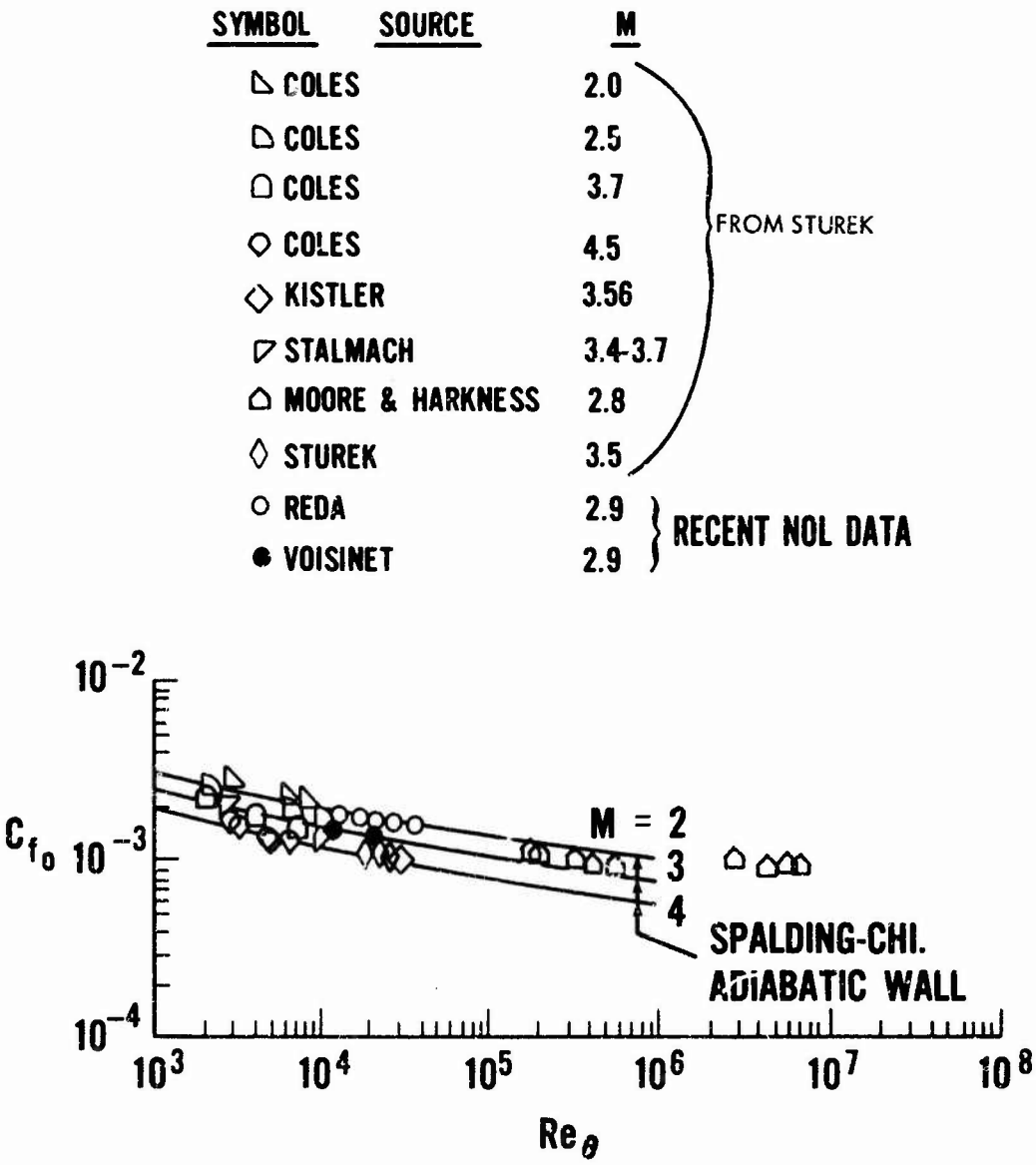

FIG. 11 SMOOTH WALL SKIN FRICTION COEFFICIENTS; A COMPARISON WITH PUBLISHED DATA

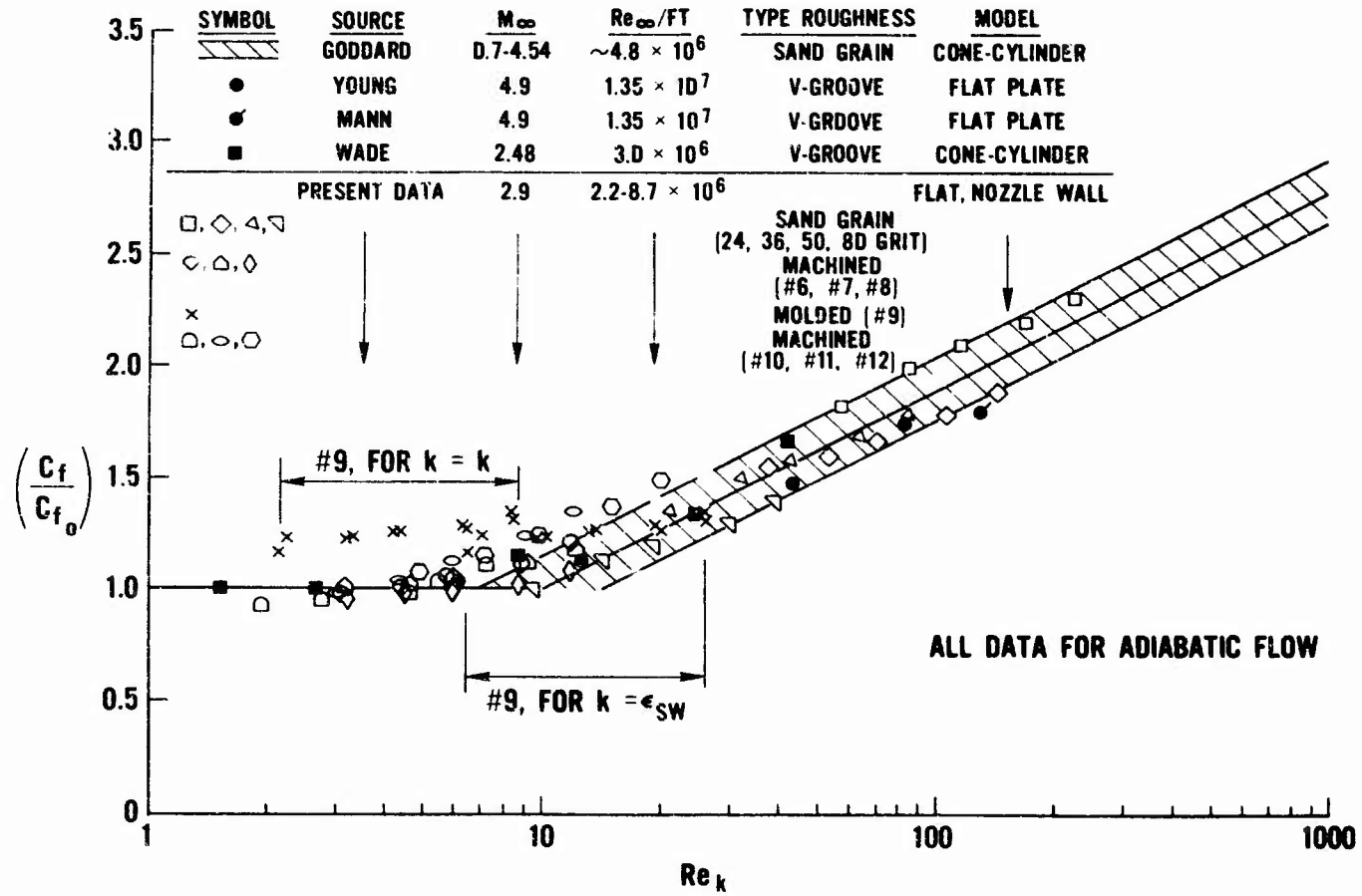

FIG. 12 SMOOTH-TO-ROUGH WALL SKIN FRICTION COEFFICIENT RATIO VS ROUGHNESS REYNOLDS NUMBER; A COMPARISON WITH PUBLISHED DATA

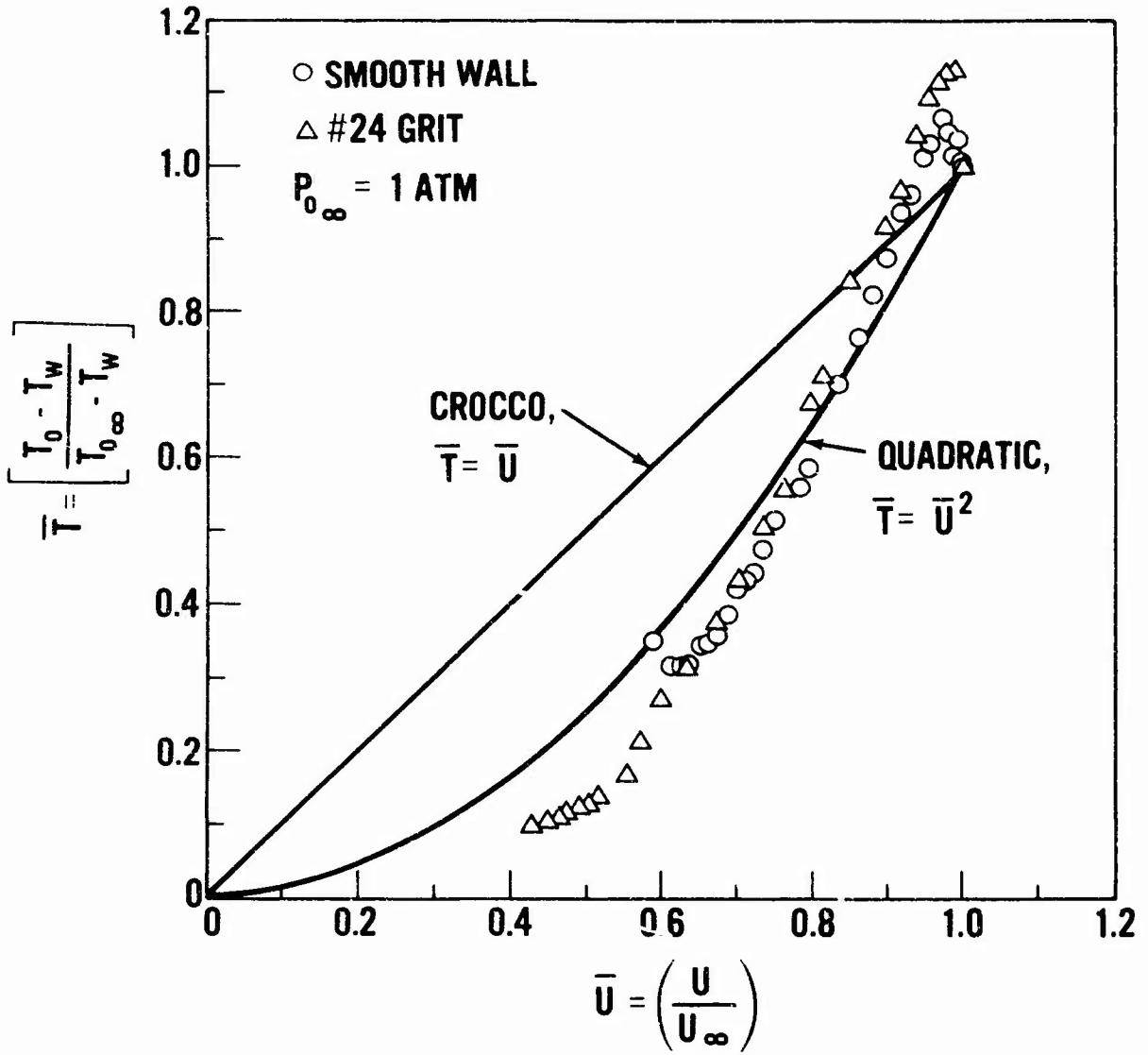

FIG. 13 SMOOTH AND ROUGH WALL RECOVERY TEMPERATURE PROFILES

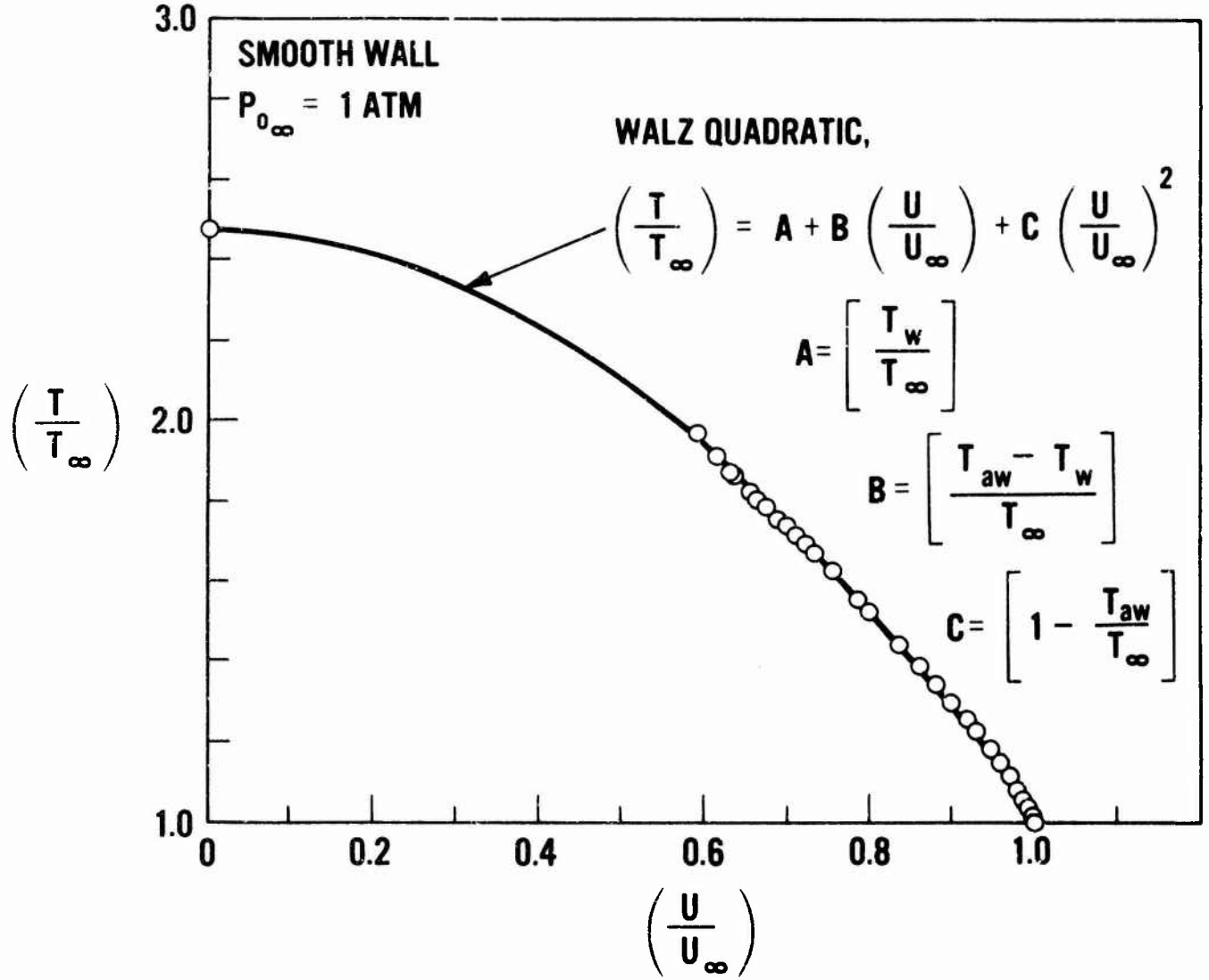

FIG. 14a SMOOTH AND ROUGH WALL TEMPERATURE-VELOCITY RELATIONSHIPS

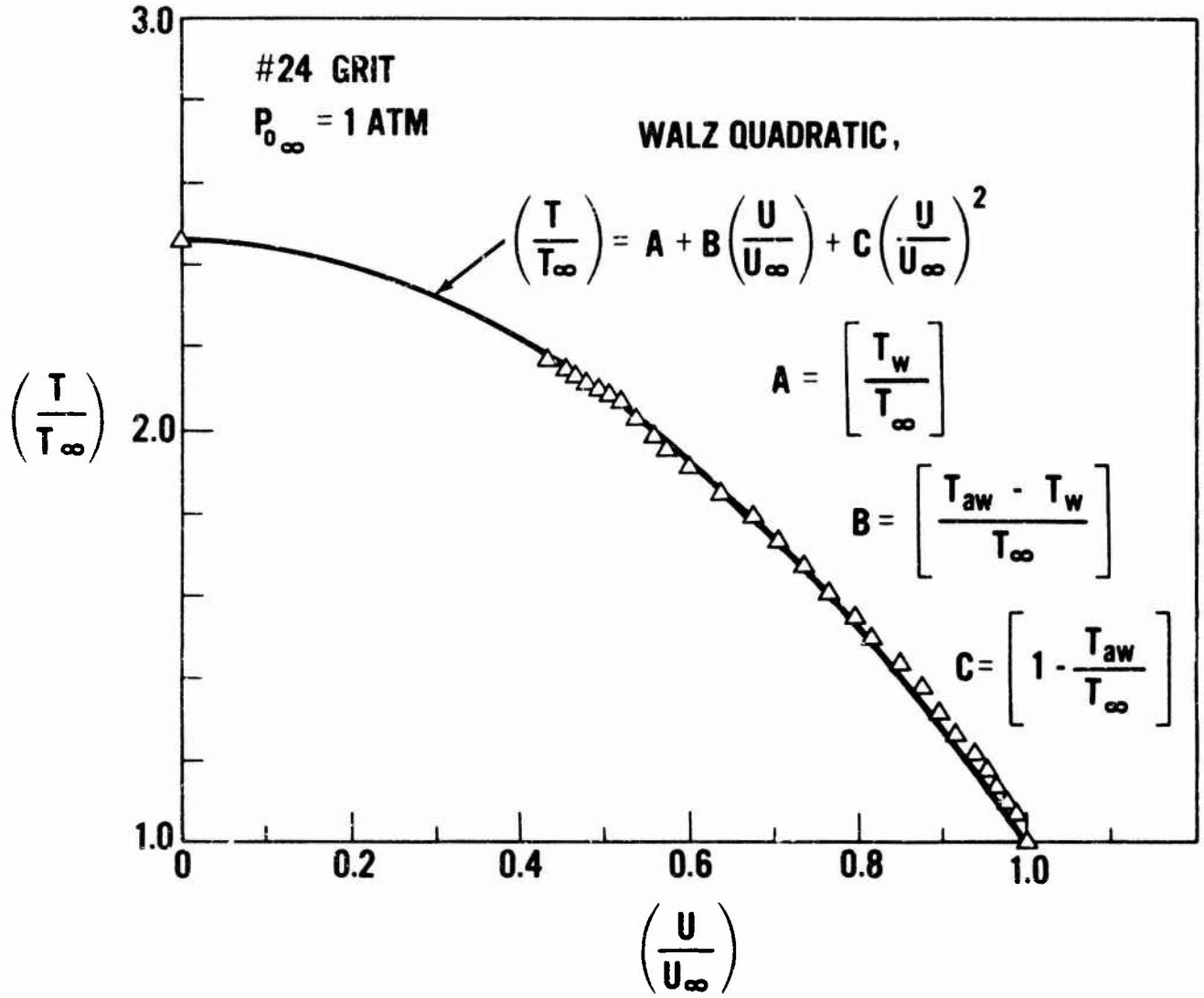

FIG. 14b SMOOTH AND ROUGH WALL TEMPERATURE-VELOCITY RELATIONSHIPS

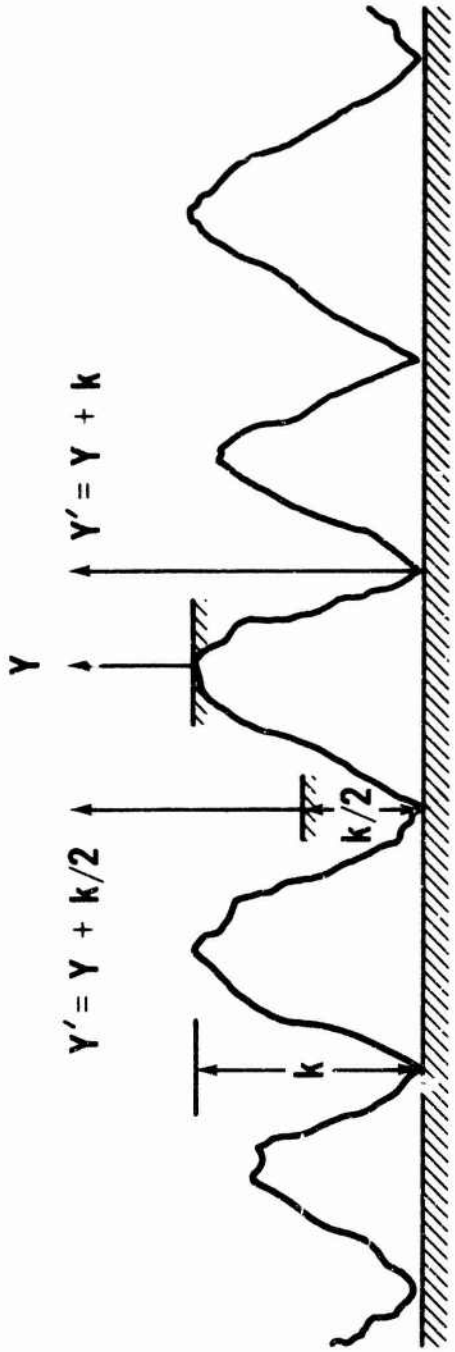

FIG. 15 EFFECTIVE y ORIGIN SCHEMATIC

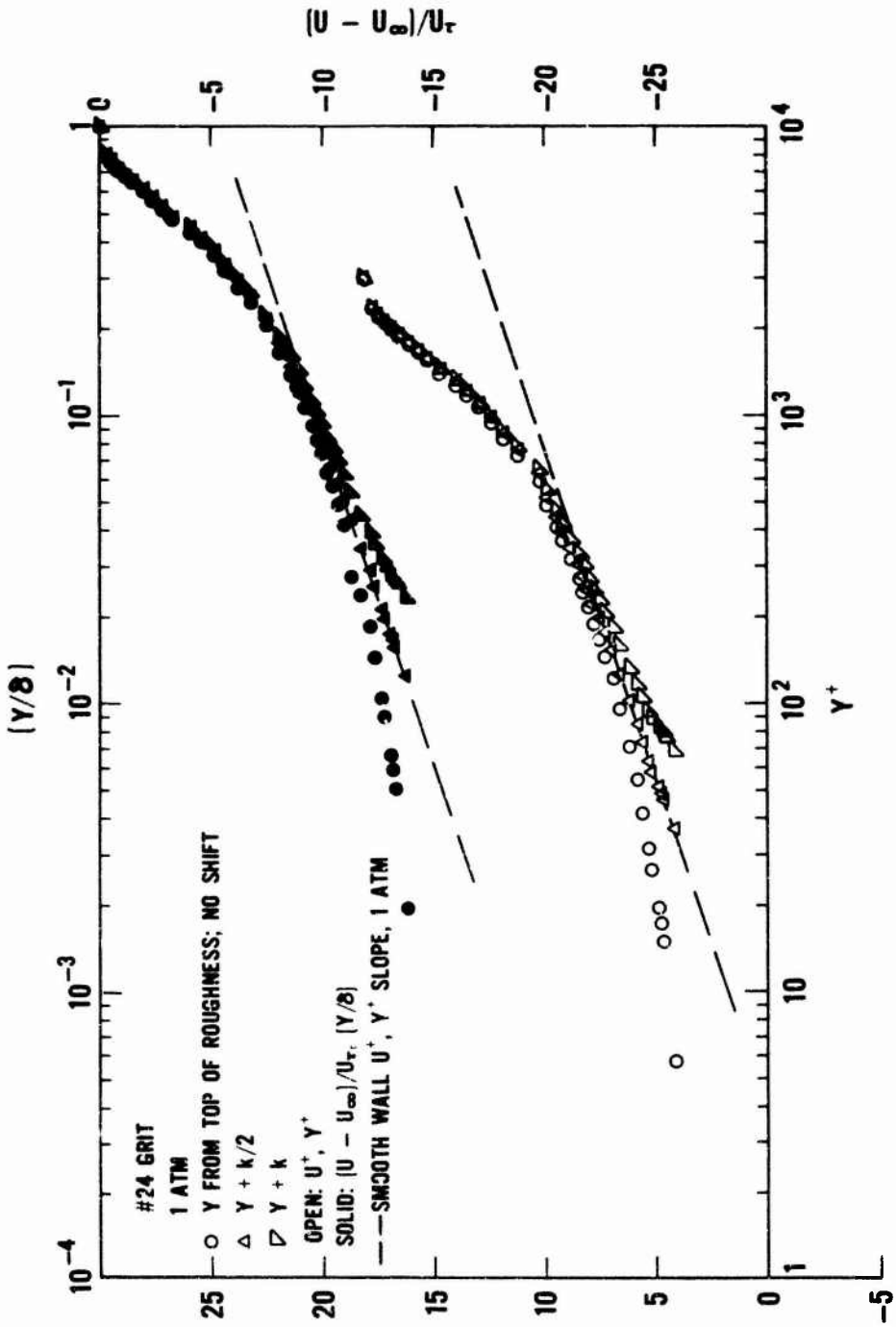

FIG. 16 EFFECTIVE y ORIGIN DEFINITION

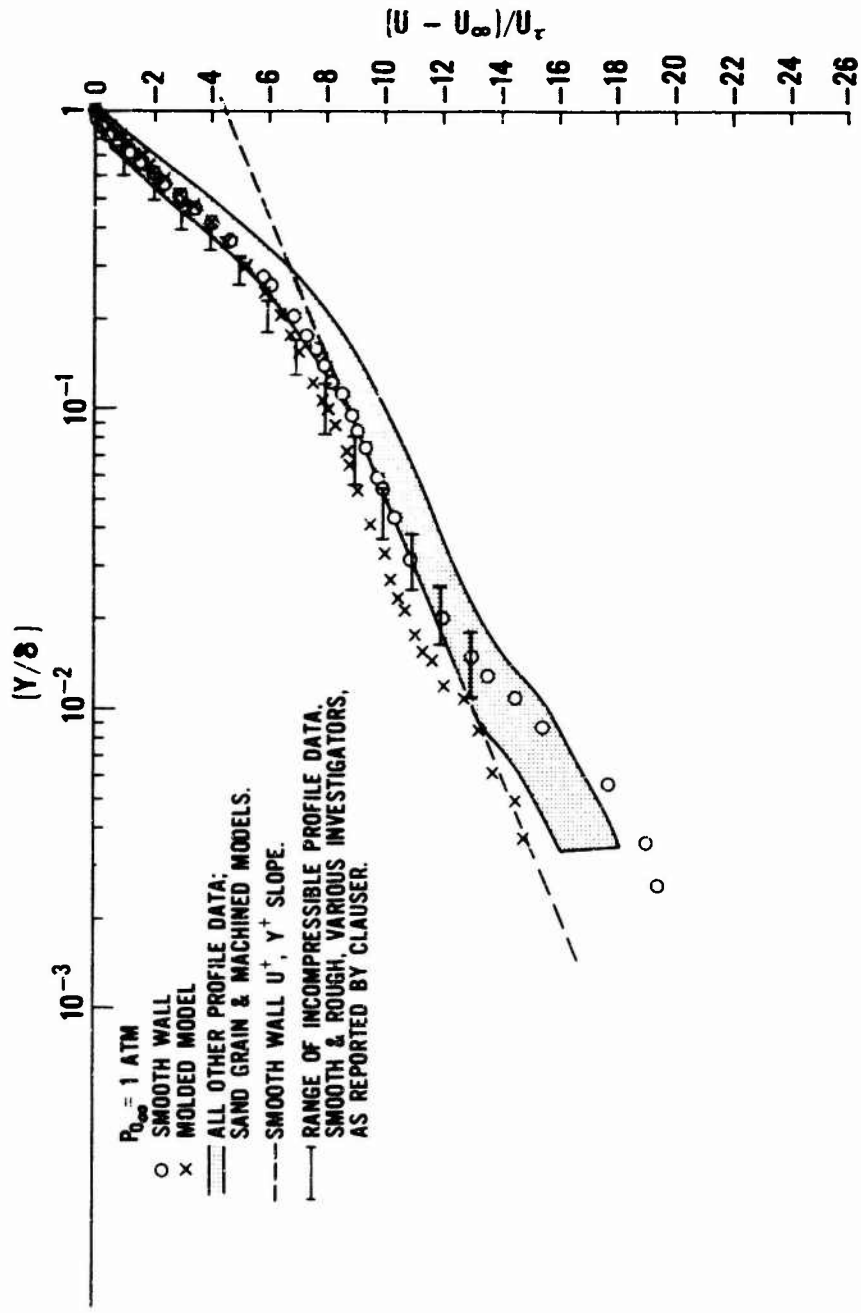

FIG. 17 VELOCITY DEFECT CORRELATION, SMOOTH AND ROUGH WALL DATA; A COMPARISON WITH PUBLISHED DATA

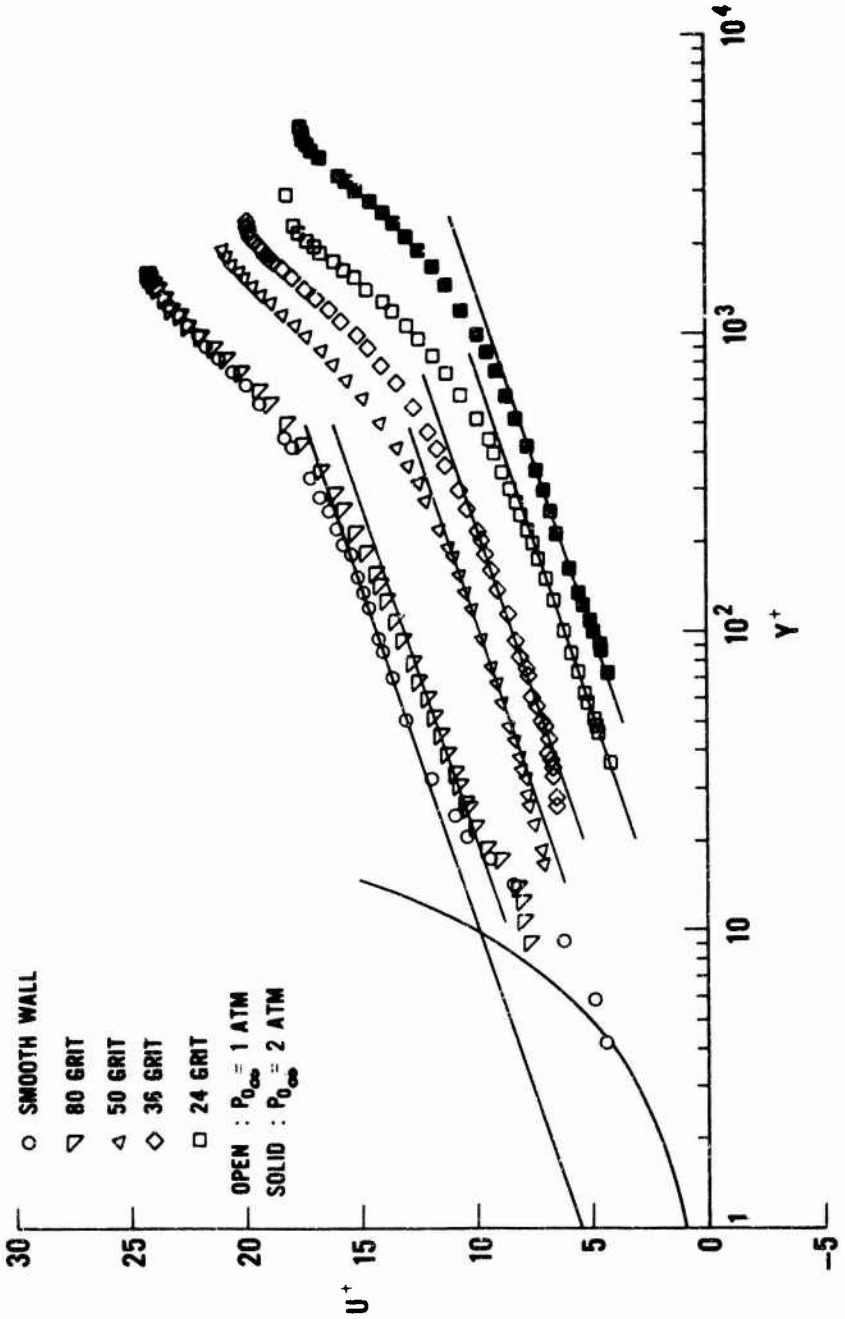

FIG. 18a SMOOTH AND ROUGH WALL VELOCITY PROFILES IN LAW-OF-THE-WALL COORDINATES

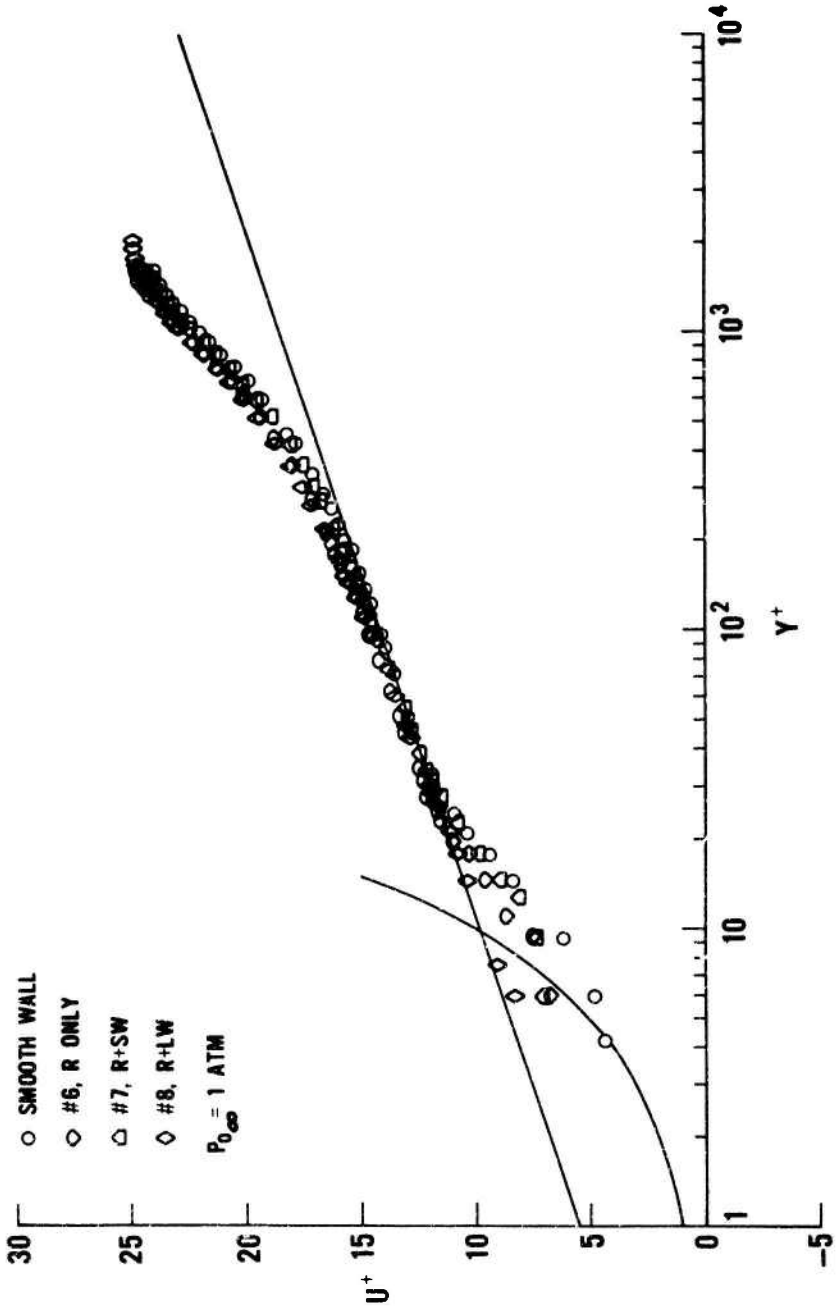

FIG. 18b SMOOTH AND ROUGH WALL VELOCITY PROFILES IN LAW-OF-THE-WALL COORDINATES

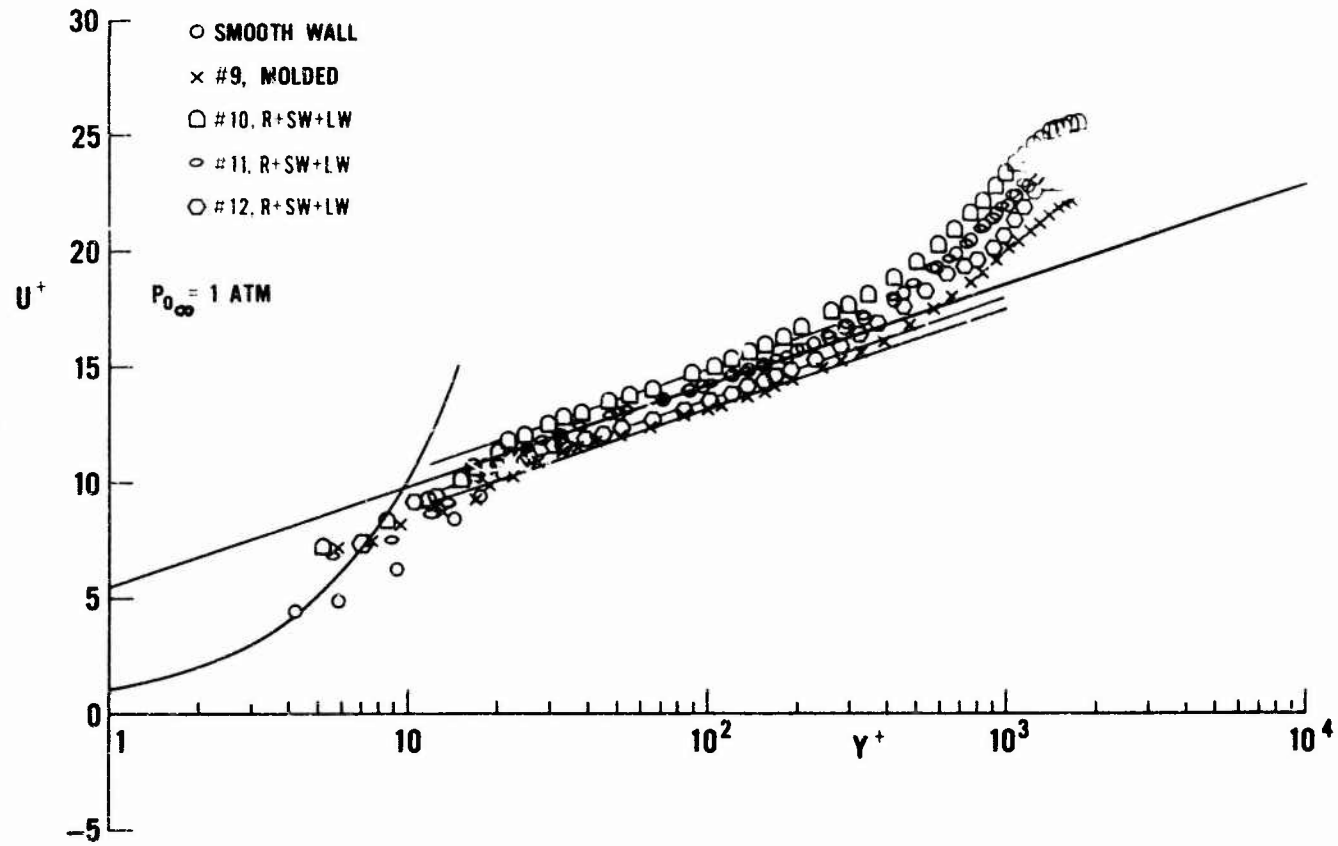

FIG. 18c SMOOTH AND ROUGH WALL VELOCITY PROFILES IN LAW-OF-THE-WALL COORDINATES

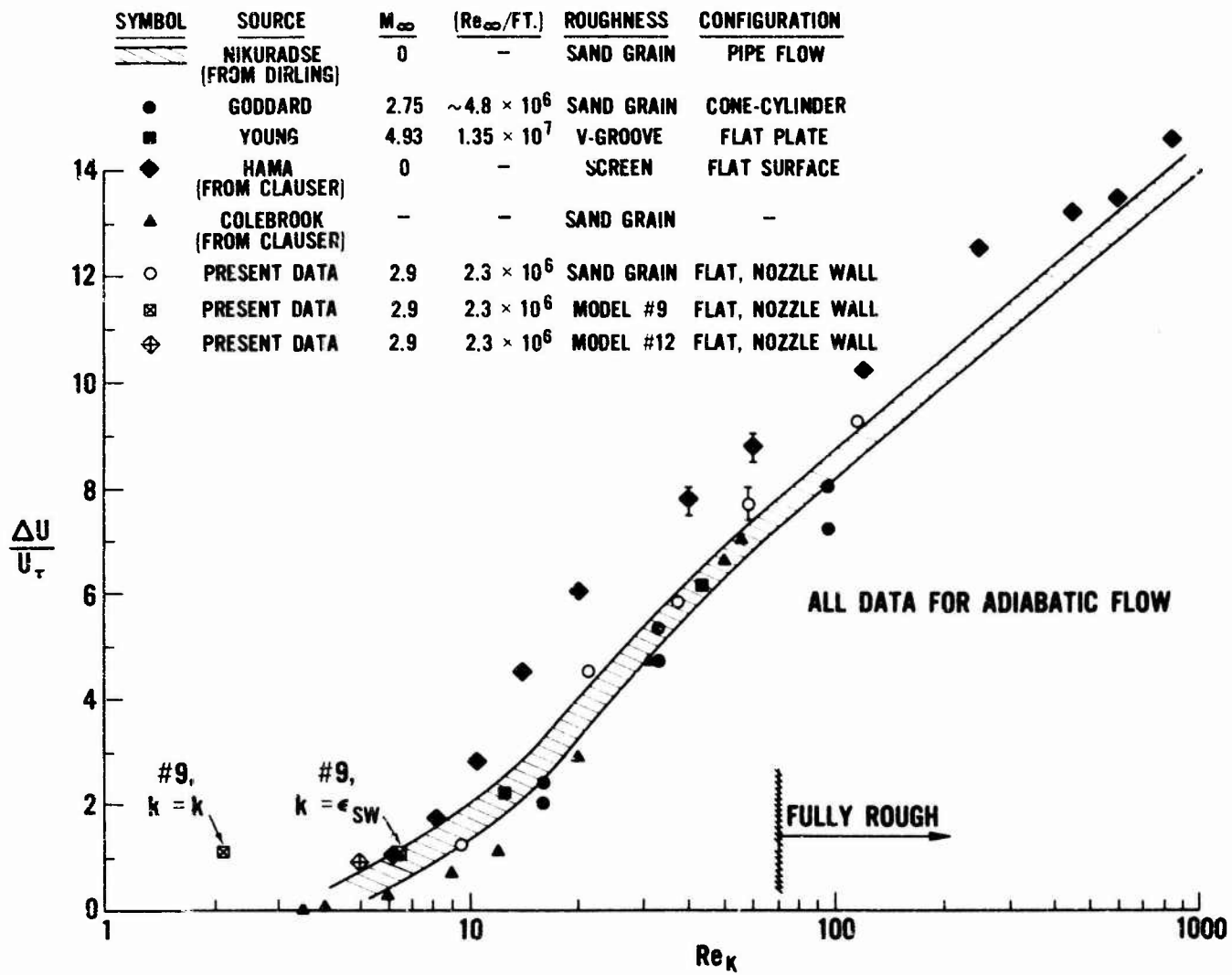

FIG. 19 ROUGHNESS INDUCED LAW-OF-THE-WALL VELOCITY SHIFT VS ROUGHNESS REYNOLDS NUMBER; A COMPARISON WITH PUBLISHED DATA

TABLE 1

SUMMARY OF MODELS TESTED

MODEL	TYPE	(k) ROUGHNESS DIMENSION (INCHES)	(ϵ_{SW}) SHORT WAVE AMPLITUDE (INCHES)	(ϵ_{LW}) LONG WAVE AMPLITUDE (INCHES)	(λ_{SW}) SHORT WAVE WAVELENGTH (INCHES)	(λ_{LW}) LONG WAVE WAVELENGTH (INCHES)	$\left(\frac{\epsilon}{\lambda}\right)_{SW}$	$\left(\frac{\epsilon}{\lambda}\right)_{LW}$
SMOOTH	MACHINED	0	0	0	0	0	–	–
24 GRIT	SAND GRAIN	.027	–	–	–	–	–	–
36 GRIT	↓	.019	–	–	–	–	–	–
50 GRIT	↓	.012	–	–	–	–	–	–
80 GRIT	↓	.006	–	–	–	–	–	–
#6	MACHINED	.002	–	–	–	–	–	–
#7	↓	.002	.004	–	0.45	–	.009	–
#8	↓	.002	–	.013	–	2.55	–	.005
#9	MOLDED	.0013	.004	.010	0.30	1.70	.013	.006
#10	MACHINED	.0013	.003	.009	0.30	1.80	.010	.005
#11	↓	.002	.004	.013	0.45	2.55	.009	.005
#12	↓	.003	.012	.026	0.79	5.40	.015	.005